NANO LETTERS

pubs.acs.org/NanoLett

Letter

Modulating Thermal Conductivity via Targeted Phonon Excitation

Xiao Wan,[▽] Dongkai Pan,[▽] Zhicheng Zong, Yangjun Qin, Jing-Tao Lü, Sebastian Volz, Lifa Zhang, and Nuo Yang*

Cite This: *Nano Lett.* 2024, 24, 6889−6896

Read Online

ACCESS | Metrics & More | Article Recommendations | Supporting Information

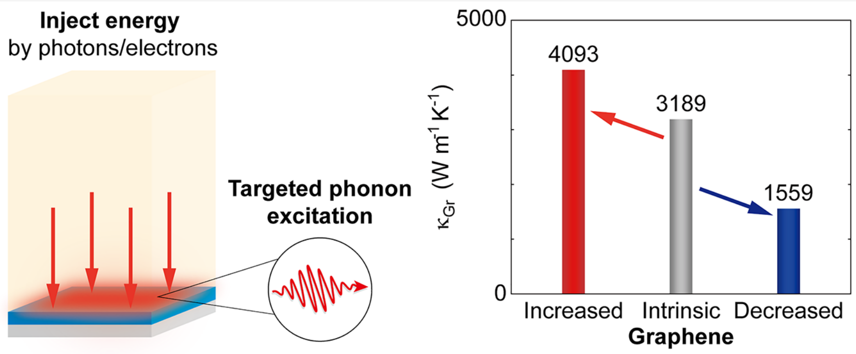

ABSTRACT: Thermal conductivity is a critical material property in numerous applications, such as those related to thermoelectric devices and heat dissipation. Effectively modulating thermal conductivity has become a great concern in the field of heat conduction. Here, a quantum modulation strategy is proposed to modulate the thermal conductivity/heat flux by exciting targeted phonons. It shows that the thermal conductivity of graphene can be tailored in the range of 1559 W m^{-1} K^{-1} (decreased to 49%) to 4093 W m^{-1} K^{-1} (increased to 128%), compared with the intrinsic value of 3189 W m^{-1} K^{-1}. The effects are also observed for graphene nanoribbons and bulk silicon. The results are obtained through both density functional theory calculations and molecular dynamics simulations. This novel modulation strategy may pave the way for quantum heat conduction.

KEYWORDS: *Thermal conductivity, Graphene, Graphene nanoribbon, Phonon*

The modulation of thermal conductivity is of great importance in various applications, including thermal managements[1−3] and energy devices.[4−6] It means that thermal conductivity, as an intrinsic property of materials, can be enhanced or decreased by an external field. And then, the heat transfer characteristics of the material are altered. Achieving desirable performances requires a deep understanding of phonon scattering mechanisms in different heat transfer regimes, which is essential to modulate the thermal conductivity of materials.[7−16] However, the complex nature of phonon transport has made the modulation of thermal conductivity a longstanding challenge in physics and material science.

Recent developments in the field of heat conduction have led to a better understanding of the scattering dynamics of heat carriers on the nanoscale. Heat conduction in dielectrics can be understood as the propagation of phonons and their scatterings such as phonon−phonon,[17,18,20] impurity,[21−23] and boundary scattering.[9,24,25] Phonon−phonon scattering has been exploited to produce weaker couplings[26−28] and to highlight hydrodynamic phonon transport[11,29] in nanostructures. Impurity scattering is highly frequency dependent and is also closely related to normal processes,[30] which can redistribute phonon frequencies and control phonon transport by nanoengineering.[1,15,21,31,32] Due to size confinement, phonon transport is largely affected by the boundary scattering,[9] resulting in the size dependence of thermal conductivity and leading to an invalid Fourier's law.[33−35]

As the understanding of phonon scattering mechanisms has advanced, a variety of new strategies to modulate the thermal conductivity have been developed, motivated by the great demand for thermal management. An enhanced thermal conductivity can be achieved by minimizing phonon−phonon scattering phase space and phonon−impurity scattering in bulk materials.[2,14,18−20,36−42] Conversely, to reduce thermal conductivity, the strategies that increase phonon scattering have been explored,[43−46] such as intrinsically increasing anharmonicity or crystal complexity or extrinsically introducing disorder, defects, boundaries, interfaces, and nanoparticles.

Received: February 15, 2024
Revised: May 7, 2024
Accepted: May 7, 2024
Published: May 13, 2024

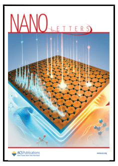

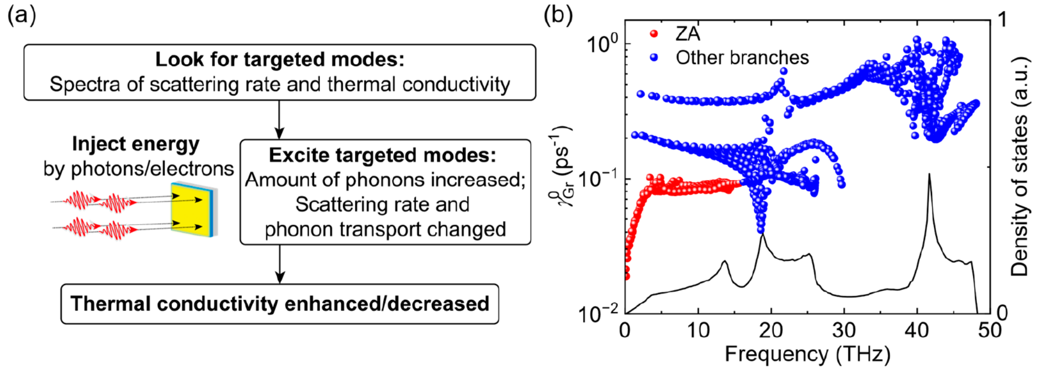

Figure 1. Modulating thermal conductivity via targeted phonon excitation. (a) Schematic of modulation strategy. (b) The density of states (DOS) and intrinsic scattering rates $\gamma^0_{\rm Gr}$ of graphene (Gr) by ab initio calculations for choosing targeted phonons. The superscript "0" represents the intrinsic value.

Besides, the wave nature of phonons[47] can also be leveraged to modulate the thermal conductivity, as seen in the development of nanophononic crystals[48−50] and the increase of tuning phonon coherence[51−53] and localization.[54−56] In recent works, external fields have been implemented to change the morphology of structures, thereby regulating thermal conductivity.[37,41,57−59] Nevertheless, while these strategies mentioned above have shown promise, they currently cannot modulate the thermal conductivity with a mode targeting ability or controllability.

Recently, there has been growing interest in targeted phonon mode excitation using terahertz optical pulses or tensile strain to modulate optical and electrical properties. The methods offer several advantages such as in situ, flexibility, quick response, and directness, without requiring any structural modification. For instance, terahertz excitation pulses have been used to directly excite optical phonons in $\mathrm{MAPbI_3}$, resulting in significant perturbations in the electron relaxation dynamics.[60] Similarly, selectively exciting vibrational modes of the molecules has been shown to modulate the performance of an organic optoelectronic system.[61] Furthermore, the nonequilibrium carrier-phonon dynamics in photovoltaic systems have been discussed in detail for a few perovskites. These discussions have revealed the quantum emission of longitudinal optical (LO) phonons, the decay of optical phonons to acoustic phonons, and other relaxation processes when abundant carriers are injected.[62−64] Nonequilibrium between optical and acoustic phonons has also been observed in photoexcited graphene and $\mathrm{MoS_2}$.[65,66] In black phosphorene, the excitation of out-of-plane acoustic phonons (ZA modes) induced by tensile strain can provide a strong modulation of the electronic band structures, carrier lifetime, and carrier mobility.[67] Additionally, targeted phonon excitation has been used to enhance ion diffusion[68] and induce structural phase transitions.[69,70] While these results demonstrate the feasibility of targeted phonon excitation, fewer studies have investigated the strategy's potential for modulating thermal conductivity.

Here, the strategy of quantum excitation of phonons is proposed to modulate the thermal conductivity of dielectric materials, where phonons dominate in the heat conduction. This strategy involves exciting targeted phonons to increase or decrease the phonon scattering, thus achieving the desired thermal conductivities. The effectiveness and capability of this strategy are demonstrated using ab initio calculations[71] and molecular dynamics simulations.[72] Graphene and graphene nanoribbon are chosen as the model systems, since the thermal conductivities of graphene and its derivatives have been extensively studied. Besides, this strategy is also validated on typical 3D bulk silicon at 150 K (see Appendix A in the Supporting Information). The results indicate that the thermal conductivity can be modulated by exciting phonons in a quantum manner without altering the structure.

The strategy aims to modulate thermal conductivity by exciting targeted phonon modes in a quantum manner, as illustrated in Figure 1a. First, the dominant modes for heat transport are identified utilizing first-principles and molecular dynamics (MD) simulations. Then, the energy of these modes is artificially increased, allowing for the quantum excitation of dominant phonons with large contributions to thermal conductivity and weak coupling with other phonons. This results in a significant enhancement of the thermal conductivity. On the other hand, if phonons with high scattering rates and relatively low contributions to thermal conductivity are excited, scattering processes are promoted, leading to a decrease in thermal conductivity. Phonon DOS determines the number of excited modes around a specific frequency, thus indicating the effectiveness of activating those modes. It is worth noting that thermal conductivity can be modulated over a wide range by exciting only a few dominant phonons without introducing other scattering mechanisms.

The method basically relies on the nature of phonon scattering. Heat conduction in solids is directly related to phonon scattering, where an individual mode can participate in various scattering processes. By identifying the characteristic time of phonon relaxation time or lifetime, τ, the thermal conductivity can be generally written as an integration as[9,10,24]

$$\kappa = \frac{1}{3}\int C(\omega)v^2(\omega)\tau(\omega)\,\mathrm{d}\omega \tag{1}$$

where the parameter 1/3 is related to the dimension of the system, $C(\omega)$ refers to the spectral volumetric specific heat, v refers to the phonon group velocity, and ω is the frequency. In general, the diverse scatterings can be incorporated into Matthiessen's rule[9,24]

$$\frac{1}{\tau} = \frac{1}{\tau_{\text{ph-ph}}} + \frac{1}{\tau_{\text{im}}} + \frac{1}{\tau_{\text{b}}} \tag{2}$$

where $\tau_{\text{ph-ph}}$, τ_{im}, and τ_{b} are the relaxation times due to phonon−phonon, impurity, and boundary scattering processes, respectively. The relaxation time of phonon−phonon scattering is calculated using Fermi's golden rule,[73] while impurity

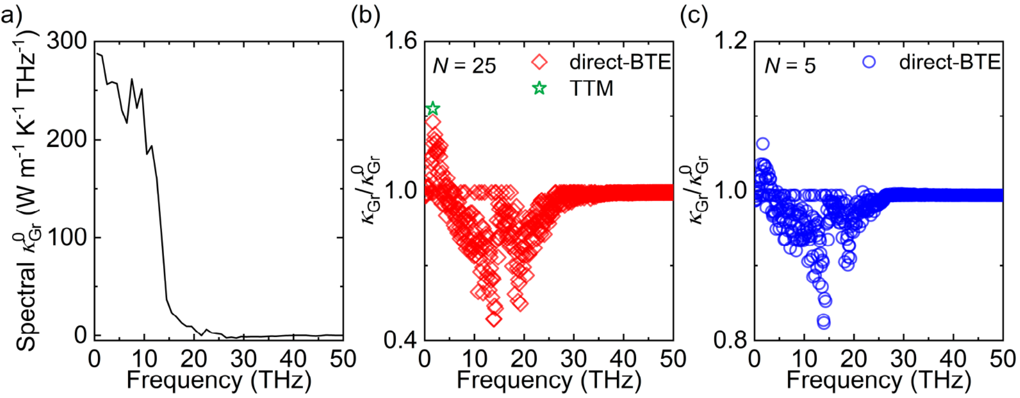

Figure 2. Thermal conductivity modulation for graphene via targeted phonon excitation. (a) Spectral contributions to k^0_{Gr} as a function of frequency. (b, c) The relative overall thermal conductivity of graphene after and before the excitation $k_{\mathrm{Gr}}/k^0_{\mathrm{Gr}}$ as a function of the center frequency for targeted phonons. For instance, the first center frequency is 0.05 THz, and a few modes in 0−0.1 THz are excited with a 25 or 5 times larger energy. The energy needed for the excitation is at most 20.8 mJ m^{-2} (N = 25) or 3.5 mJ m^{-2} (N = 5).

scattering can be attained based on Klemens' derivation.[9] In addition, crystal boundary scattering is determined by diffuse boundary absorption/emission, which depends on the Casimir length. It is important to note that impurity and boundary scatterings are not included in the calculation of this work.

By increasing the energy of targeted phonons, the scattering rate can be changed significantly, leading to modulation of the thermal conductivity. To change the energy of mode n, the phonon occupation numbers are modified in ab initio calculations according to the formulation

$$E'_n = \hbar\omega_n \frac{N}{e^{\hbar\omega_n/k_{\mathrm{B}}T} - 1} \tag{3}$$

where E'_n corresponds to the energy of mode n after the modification, $\hbar$ denotes the reduced Planck constant, k_{B} is the Boltzmann constant, T is the absolute lattice temperature, and N represents the multiple of energy increase.

In MD simulations, the value of N can be calculated as $\langle E'_n\rangle/\langle E_n\rangle$, which is the ratio of the mode energy after and before excitations. It is difficult to directly increase the mode energy to N times its original value in the simulation. Therefore, the atomic velocities (kinetic energy) are chosen to be rescaled according to the formulation (derivation in Appendix C in the Supporting Information)

$$v'_j = v_j + \frac{1}{\sqrt{m_j}}(\sqrt{M} - 1)\dot{Q}_n(t)\boldsymbol{e}_{j,n} \tag{4}$$

where v'_j and v_j are the velocities of atom j after and before excitations, respectively, m_j is the atomic mass, $\dot{Q}_n$ is the normal mode velocity coordinate, and $\boldsymbol{e}_{j,n}$ is the eigenvector. Equation 4 implies that the mode kinetic energy $E_{n,K}$ is increased by M times. The rescale factor M is set to 10. Due to the conversion between kinetic and potential energy, as well as the evolution and diffusion, the actual multiple of energy increase N is around one-third of M (depicted in Figure S10).

The effectiveness of the strategy is demonstrated in both graphene and graphene nanoribbon systems. However, it is worth noting that this approach could be applicable to other systems with weak-coupling phonons.[26−28] Ab initio calculations (details in Appendix A in the Supporting Information) for graphene are performed using the Vienna ab initio simulation package (VASP),[74] and the phonon transport properties are obtained by solving the phonon Boltzmann transport equation with the special version of ShengBTE packages modified by Ruan et al., which has better convergence over two-dimensional materials,[75,76] assisted by the PHONOPY package.[77] Additionally, nonequilibrium molecular dynamics (NEMD, details in Appendix B in the Supporting Information) simulations for graphene nanoribbon are conducted using the LAMMPS package.[78]

Indeed, the specific implementation of this strategy in experimental settings is also an important and notable consideration. The selection of appropriate excitation methods depends on the specific phonons that are being targeted. Here are some brief descriptions to provide further clarity. In the case of optical phonons, for instance, they can be effectively excited by illuminating the sample with THz pulses using a tabletop light source, which are generated by optical rectification using the tilted-pulse-intensity-front scheme. The intensity of the THz pulse can be controlled by a pair of wire grid polarizers operating in the THz frequency region, as described in ref 60. Ideally, the frequency of the illuminated photons should be close to the THz magnitude, corresponding to the "targeted phonons" indicated in the thermal conductivity spectrum in Figure 2a. Techniques such as THz time domain spectroscopy (THz-TDS) can be utilized to detect any enhanced signal caused by external stimuli and compare it to the baseline (no shining) performance. Besides, in the study by Wu et al.,[79] an out-of-plane acoustic phonon is selectively excited in graphene by a different approach, scanning tunneling spectroscopy. To this end, the tunneling current was passed through a molecule adsorbed on graphene on a metal surface. The rich structure observed in the experimental inelastic electron tunneling spectra could be reproduced by nonequilibrium transport calculations. Importantly, besides the presence of spectroscopic signals due to molecular vibrational quanta, graphene phonon excitation also left its footprint in the spectra, too. This showed that the coupling of symmetry-equivalent and energetically similar vibrational modes of the molecule and graphene led to the selective excitation of a specific acoustic graphene phonon, which without the molecule remained below the detection limit. Therefore, these recent experimental findings are very encouraging and pave the way for selectively exciting targeted phonons.

First, the spectral contribution to intrinsic thermal conductivity of graphene k^0_{Gr} is calculated as a guidance to

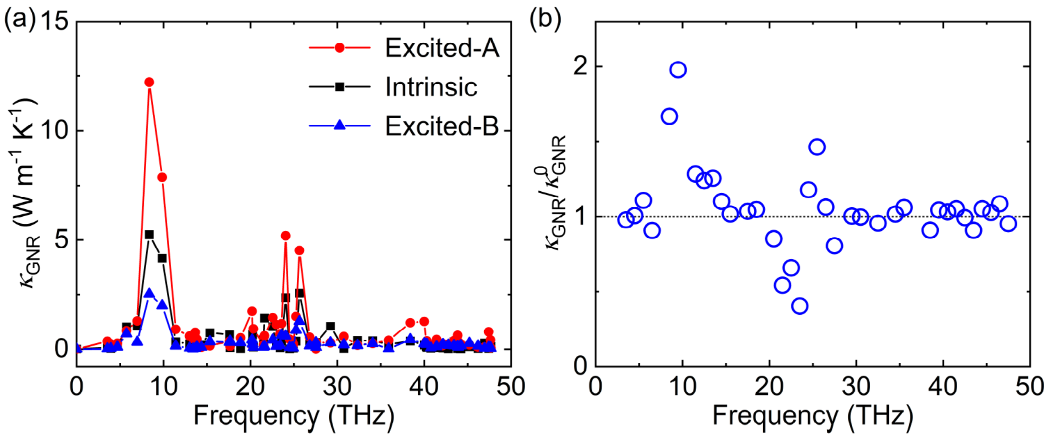

Figure 3. Thermal conductivity modulation for graphene nanoribbon (GNR) via targeted excitation of phonons. (a) Thermal conductivity contribution spectrum by molecular dynamics simulations, "A" refers to the case where two modes, 9.84 THz, $\boldsymbol{k} = (-0.64, 0.96, 0)$ and 9.84 THz, $\boldsymbol{k} = (0.64, -0.96, 0)$, are excited with a 3.34 times larger kinetic energy ($N = 3.34$), and "B" represents the case where four modes, 23.59 THz, $\boldsymbol{k} = (-0.64, 0.37, 0)$, 23.41 THz, $k = (-0.64, 0.66, 0)$, 23.41 THz, $\boldsymbol{k} = (0.64, -0.66, 0)$, $\boldsymbol{k} = (0.64, -0.66, 0)$, and 23.59 THz, $\boldsymbol{k} = (0.64, -0.37, 0)$, are excited with $N = 2.71$. $\boldsymbol{k}$ represents the wave vector. (b) Relative thermal conductivity of the graphene nanoribbon after and before the excitation k_{GNR}/k^0_{GNR} by exciting a few modes in each 1 THz frequency range utilizing molecular dynamics simulations.

highlight the effectiveness of the modulation strategy, as shown in Figure 2a. An iterative solving method is utilized to accurately solve the Boltzmann transport equation.[75] The obtained value for k^0_{Gr} at 300 K is 3189 W m^{-1} K^{-1}, which is comparable to those in previous works (1500−4000 W m^{-1} K^{-1}).[80−84] Figure 2a suggests that the low-frequency modes dominate the heat conduction in graphene, particularly those below 5 THz and around 10 THz. The spectral k^0_{Gr} decreases drastically in the higher frequency range, indicating a negligible contribution of these modes to heat conduction. This observation provides a prominent information for selecting the modes to be adjusted in energy.

Then, the energy is injected to excite more heat carriers into the dominant modes. However, it can be observed from Figure 2b that the results do not correspond perfectly to the tendency shown in Figure 2a, since the DOS and scattering rates are also essential factors in implementing the modification, as illustrated in Figure 1b. The DOS determines the number of modes that can be affected during excitation, while a high scattering rate means that the modes are strongly scattered, leading to a smaller contribution to heat conduction and a larger resistance of other modes. In graphene, ZA modes play a much more significant role in heat conduction due to the symmetry-based selection rule.[83] The reflection symmetry of its 2D structure excludes all the 3-phonon scatterings that involve odd numbers of flexural phonons, causing a profound reduction in the scattering rates of flexural modes, especially ZA modes. Thus, exciting those modes can generate more noticeable effects. As a result, the peak of k_{Gr}/k^0_{Gr} located at around 1.7 THz (k_{Gr} is the thermal conductivity of graphene after excitation) ensures a high enough DOS and a low scattering rate, as well as a high spectral thermal conductivity. On the other hand, the trough is situated around 13.9 THz, close to the maximum frequency of the ZA phonon branch, ensuring a high enough DOS, a relatively high scattering rate, and small spectral thermal conductivity compared to other ZA modes. The scattering rates' changes after and before the excitation are also presented in Appendix A in the Supporting Information.

An alternative method has been incorporated to validate the modulation results obtained by the previously discussed direct-BTE method. This alternative approach is termed the two-temperature model (TTM), which considers the nonequilibrium between the excited phonon group and the intrinsic phonon group (details in Appendix D in the Supporting Information). The two-temperature model is widely utilized to address weak coupling systems, including electron−phonon, phonon−phonon, and phonon−magnon couplings.[25,26,85,86] To streamline the calculations, it is valuable to focus specifically on the peak case to avoid redundancy. It is notable that the results obtained using the two-temperature model closely correspond to those from the previous method, and interestingly, the two-temperature model demonstrates an even more pronounced modulation effect.

Molecular dynamics simulations are conducted on graphene nanoribbons to validate the feasibility of the modulation strategy, especially considering high-order scatterings. As shown in Figure 3a, the thermal conductivity contribution spectra of graphene nanoribbon (24.9 × 21.6 Å^2) are extracted through NEMD simulations.[87,88] The intrinsic thermal conductivity of graphene nanoribbon k^0_{GNR} at 300 K is 59.0 W m^{-1} K^{-1}, which is consistent with previous studies.[49] Due to the limitation in the simulation cell size, the possible excited phonons have smaller wavelengths and higher frequencies (above 3 THz). The thermal conductivity contribution spectrum is obtained by extracting time-dependent atomic motion data in the intermediate region where the temperature difference remains small (<0.3 K in all the cases) to ensure the validity of the lattice dynamic method. The excitation region is chosen to be all parts of the simulation cell except for the heat sink and fixed region, with the additional heat flux generated by the excitation being relatively small (2−5%) compared to the heat flux generated by the Langevin thermostat (Figure S11 in Appendix B in the Supporting Information). The excitation is conducted every 100 fs with an equivalent input energy density of 0.21−0.48 mJ m^{-2}. The overall thermal conductivity refers to an effective quantity measuring heat flux. It should also be noted that there are only a few modes in each 1 THz frequency range, which accounts for 2−7% of all modes of the Brillouin zone. Moreover, modes around 10 THz make a significant contribution to the intrinsic thermal conductivity, as shown in Figure 3a. In particular, selecting two modes between 9 and 10

THz as targeted phonons (excited-A) results in a considerable increase in the overall thermal conductivity, with a 97.8% enhancement (from 59.0 to 116.7 W m^{-1} K^{-1}) when those modes are excited with N = 3.34 (3.34 times larger kinetic energy). Figure 3a also shows the thermal conductivity contribution after the excitation. It can be concluded that the increase of k_{GNR} (the thermal conductivity of graphene nanoribbon after excitation) is mainly contributed from modes below 10 THz and modes in the 24−26 THz range, with the contribution of these modes not changing significantly compared to the original value. Furthermore, targeted phonons in other frequency ranges are also excited in a similar manner, as shown in Figure 3b. The excitation of these modes regulates the overall thermal conductivity by different ratios. The modes between 9 and 10 THz show the highest modulation ratio, owing to high contribution to k_{GNR}, with the modes in the 25−26 THz range showing similar behavior. In general, the enhancement of k_{GNR} decreases with increasing frequency (below 15 THz). This can be attributed to higher phonon density of states (DOS) in the high-frequency range.

The modulation results of NEMD simulations for decreasing k_{GNR} exhibit a tendency similar to that of the ab initio calculations. In Figure 3a, modes in the 15−24 THz range show low contribution to k_{GNR}. When four modes between 23 and 24 THz are excited with a 2.71 times larger kinetic energy (excited-B, N = 2.71), k_{GNR} decreases by 59.6% (from 59.0 to 23.8 W m^{-1} K^{-1}). The comparison before and after the excitation is shown in Figure 3a. The contribution of modes to k_{GNR} decreases over a wide frequency range with a greater reduction below 10 THz due to the large original contribution values. Additionally, exciting the modes in the frequencies between 20 and 24 THz also reduces k_{GNR} (from 85.1% to 40.4%), as illustrated in Figure 3b. The reduction of k_{GNR} is significant and decreases as the frequency of targeted phonons increases (below 24 THz). This trend can be related to high intrinsic scattering rates and low phonon DOS of modes around 23 THz compared to other modes.

Generally, the thermal conductivity of dielectric materials can be finely tuned based on the specific characteristics of phonon transport. For example, the introduction of ^{13}C can result in roughly a 50% reduction in thermal conductivity compared to isotopically pure graphene, attributed to strong phonon-point defect scattering.[89] In the case of graphene nanoribbons, phonon transport can be hindered by local resonant hybridization from nanostructures on the sides, leading to a 73% reduction in thermal conductivity.[49] Additionally, strain can alter thermal transport properties by affecting the morphology. For instance, when the compressive strain reaches 0.08, the thermal conductivity of graphene decreases by about 45% due to structural buckling.[90] While these methods can achieve considerable regulatory results, they are not in situ and require structural modification or deformation. Comparatively, the targeted phonon excitation strategy can not only effectively reduce thermal conductivity but also represent a very promising direction for enhancing thermal transport in addition to reducing impurity scattering.

Defects in materials, such as impurities or isotopes, also have a crucial effect on the regulation results. The effect of targeted phonon excitation is contingent upon a competitive mechanism, which induces changes in the scattering rates and heat transfer pathways. When defect scattering is introduced, the intrinsic thermal conductivity can be reduced. Then, both the modulation results in the peak and trough cases after excitation might decrease. In analytical models, the phonon-defect scattering rate is typically approximated as $\sim\omega^4$,[91] exhibiting a less pronounced frequency dependence in graphene.[92,93] This implies that higher frequency phonons experience stronger scattering compared to lower frequency phonons. Consequently, the peak in the thermal conductivity modulation might shift toward lower frequencies, while the trough might shift toward higher frequencies. Nevertheless, the overall trend of regulation remains unchanged. Besides, other types of scattering work in a similar way, e.g., boundary scattering. Therefore, the introduction of defect scattering does not alter the overall trend of relative thermal conductivity concerning the frequency of targeted phonons. But it affects the specific modulation range, as well as the positions of the peak and trough.

In this work, a new strategy for modulating thermal conductivity is proposed that is realized by exciting targeted phonons in a quantum manner. The results demonstrate that this strategy can effectively modulate the thermal conductivity of graphene and graphene nanoribbons over a wide range compared to their intrinsic values. Ab initio calculations and NEMD simulations provide detailed validation for the strategy. First, the modes with top-contribution or strong-scattering are identified; then, the energy of some of these modes is artificially increased. It is worth noting that the feasibility of this strategy has a high possibility to be confirmed experimentally.[60,61,70,79] This is because the quantum excitation of vibrational modes has already been used to modulate transport properties and induce structural phase transitions.[61,67,68,70]

This strategy represents a substantial advancement in modulating thermal conductivity/heat flux among various dielectric materials. More profoundly, it significantly contributes to the understanding of phonon transport in low-dimensional systems. And targeted phonon excitation holds crucial significance for the thermal management of electronic devices, while also paving the way for the development of thermal functional devices. In addition, by substantially reducing the thermal conductivity, it offers a novel avenue to enhance thermoelectric efficiency.

■ ASSOCIATED CONTENT

Supporting Information

The Supporting Information is available free of charge at https://pubs.acs.org/doi/10.1021/acs.nanolett.4c00478.

Additional ab initio calculation details, molecular dynamics simulation setup, derivation of the velocity rescaling formula, and derivation of the two-temperature model (PDF)

■ AUTHOR INFORMATION

Corresponding Author

Nuo Yang − *School of Energy and Power Engineering, Huazhong University of Science and Technology, Wuhan 430074, People's Republic of China; Department of Physics, National University of Defense Technology, Changsha 410073, People's Republic of China;* orcid.org/0000-0003-0973-1718; Email: nuo@hust.edu.cn, nuo@nudt.edu.cn

Authors

Xiao Wan – *School of Energy and Power Engineering, Huazhong University of Science and Technology, Wuhan 430074, People's Republic of China*

Dongkai Pan – *School of Energy and Power Engineering, Huazhong University of Science and Technology, Wuhan 430074, People's Republic of China*

Zhicheng Zong – *School of Energy and Power Engineering, Huazhong University of Science and Technology, Wuhan 430074, People's Republic of China*

Yangjun Qin – *School of Energy and Power Engineering, Huazhong University of Science and Technology, Wuhan 430074, People's Republic of China*

Jing-Tao Lü – *School of Physics and Wuhan National High Magnetic Field Center, Huazhong University of Science and Technology, Wuhan 430074, People's Republic of China*

Sebastian Volz – *LIMMS, CNRS-IIS UMI 2820, The University of Tokyo, Tokyo 153-8505, Japan; Institute of Industrial Science, The University of Tokyo, Tokyo 153-8505, Japan*

Lifa Zhang – *Phonon Engineering Research Center of Jiangsu Province, Ministry of Education Key Laboratory of NSLSCS, Center for Quantum Transport and Thermal Energy Science, Institute of Physics Frontiers and Interdisciplinary Sciences, School of Physics and Technology, Nanjing Normal University, Nanjing 210023, People's Republic of China;* orcid.org/0000-0001-6108-1404

Complete contact information is available at:
https://pubs.acs.org/10.1021/acs.nanolett.4c00478

Author Contributions

$^{\nabla}$X.W. and D.P. contributed equally to this work.

Notes

The authors declare no competing financial interest.

ACKNOWLEDGMENTS

This work was sponsored by the National Key Research and Development Project of China, No. 2018YFE0127800. We are grateful to Jörg Kröger, Zhengyou Liu, Junichiro Shiomi, Shouhang Li, Wu Li, Xiaokun Gu, and Lina Yang for helpful discussions. The authors thank the National Supercomputing Center in Tianjin (NSCC-TJ) and the China Scientific Computing Grid (ScGrid) for providing assistance in computations.

REFERENCES

(1) Qian, X.; Zhou, J.; Chen, G. Phonon-engineered extreme thermal conductivity materials. *Nat. Mater.* **2021**, *20*, 1188–1202.

(2) Huang, C.; Qian, X.; Yang, R. Thermal conductivity of polymers and polymer nanocomposites. *Materials Science and Engineering: R: Reports* **2018**, *132*, 1–22.

(3) Xu, X.; Chen, J.; Zhou, J.; Li, B. Thermal Conductivity of Polymers and Their Nanocomposites. *Adv. Mater.* **2018**, *30* (17), 1705544.

(4) Mao, J.; Chen, G.; Ren, Z. Thermoelectric cooling materials. *Nat. Mater.* **2021**, *20* (4), 454–461.

(5) Dresselhaus, M. S.; Chen, G.; Tang, M. Y.; Yang, R. G.; Lee, H.; Wang, D. Z.; Ren, Z. F.; Fleurial, J. P.; Gogna, P. New Directions for Low-Dimensional Thermoelectric Materials. *Adv. Mater.* **2007**, *19* (8), 1043–1053.

(6) Cahill, D. G.; Braun, P. V.; Chen, G.; Clarke, D. R.; Fan, S.; Goodson, K. E.; Keblinski, P.; King, W. P.; Mahan, G. D.; Majumdar, A.; Maris, H. J.; Phillpot, S. R.; Pop, E.; Shi, L. Nanoscale thermal transport, II. 2003–2012. *Applied Physics Reviews* **2014**, *1* (1), 011305.

(7) Allen, P. B.; Feldman, J. L. Thermal conductivity of disordered harmonic solids. *Phys. Rev. B* **1993**, *48* (17), 12581–12588.

(8) Dove, M. T. *Introduction to Lattice Dynamics*; Cambridge University Press: 1993.

(9) Chen, G. *Nanoscale energy transport and conversion: a parallel treatment of electrons, molecules, phonons, and photons*; Oxford University Press: 2005.

(10) Kittel, C. *Introduction to solid state physics*, 7th ed.; Wiley: 1996.

(11) Chen, G. Non-Fourier phonon heat conduction at the microscale and nanoscale. *Nature Reviews Physics* **2021**, *3* (8), 555–569.

(12) Chen, G.; Zeng, T.; Borca-Tasciuc, T.; Song, D. Phonon engineering in nanostructures for solid-state energy conversion. *Materials Science and Engineering: A* **2000**, *292* (2), 155–161.

(13) Li, N.; Ren, J.; Wang, L.; Zhang, G.; Hänggi, P.; Li, B. Colloquium: Phononics: Manipulating heat flow with electronic analogs and beyond. *Rev. Mod. Phys.* **2012**, *84* (3), 1045–1066.

(14) Gu, X.; Wei, Y.; Yin, X.; Li, B.; Yang, R. Colloquium: Phononic thermal properties of two-dimensional materials. *Rev. Mod. Phys.* **2018**, *90* (4), 041002.

(15) Liu, Y.; Ren, W.; An, M.; Dong, L.; Gao, L.; Shai, X.; Wei, T.; Nie, L.; Hu, S.; Zeng, C. A Qualitative Study of the Disorder Effect on the Phonon Transport in a Two-Dimensional Graphene/h-BN Heterostructure. *Frontiers in Materials* **2022**, *9*, 913764.

(16) Zhu, G.-p.; Zhao, C.-w.; Wang, X.-w.; Wang, J. Tuning Thermal Conductivity in Si Nanowires with Patterned Structures. *Chin. Phys. Lett.* **2021**, *38* (2), 024401.

(17) Lindsay, L.; Broido, D. A.; Reinecke, T. L. First-Principles Determination of Ultrahigh Thermal Conductivity of Boron Arsenide: A Competitor for Diamond? *Phys. Rev. Lett.* **2013**, *111* (2), 025901.

(18) Kang, J. S.; Li, M.; Wu, H.; Nguyen, H.; Hu, Y. Experimental observation of high thermal conductivity in boron arsenide. *Science* **2018**, *361* (6402), 575–578.

(19) Li, S.; Zheng, Q.; Lv, Y.; Liu, X.; Wang, X.; Huang, P. Y.; Cahill, D. G.; Lv, B. High thermal conductivity in cubic boron arsenide crystals. *Science* **2018**, *361* (6402), 579–581.

(20) Tian, F.; Song, B.; Chen, X.; Ravichandran, N. K.; Lv, Y.; Chen, K.; Sullivan, S.; Kim, J.; Zhou, Y.; Liu, T.-H.; Goni, M.; Ding, Z.; Sun, J.; Udalamatta Gamage, G. A. G.; Sun, H.; Ziyaee, H.; Huyan, S.; Deng, L.; Zhou, J.; Schmidt, A. J.; Chen, S.; Chu, C.-W.; Huang, P. Y.; Broido, D.; Shi, L.; Chen, G.; Ren, Z. Unusual high thermal conductivity in boron arsenide bulk crystals. *Science* **2018**, *361* (6402), 582.

(21) Kim, W. Strategies for engineering phonon transport in thermoelectrics. *Journal of Materials Chemistry C* **2015**, *3* (40), 10336–10348.

(22) Feng, T.; Qiu, B.; Ruan, X. Coupling between phonon-phonon and phonon-impurity scattering: A critical revisit of the spectral Matthiessen's rule. *Phys. Rev. B* **2015**, *92* (23), 235206.

(23) Liu, Z.; Mao, J.; Liu, T.-H.; Chen, G.; Ren, Z. Nano-microstructural control of phonon engineering for thermoelectric energy harvesting. *MRS Bull.* **2018**, *43* (3), 181–186.

(24) Tien, C. L. *Microscale energy transfer*; CRC Press: 1997.

(25) Chen, J.; Xu, X.; Zhou, J.; Li, B. Interfacial thermal resistance: Past, present, and future. *Rev. Mod. Phys.* **2022**, *94* (2), 025002.

(26) An, M.; Song, Q.; Yu, X.; Meng, H.; Ma, D.; Li, R.; Jin, Z.; Huang, B.; Yang, N. Generalized Two-Temperature Model for Coupled Phonons in Nanosized Graphene. *Nano Lett.* **2017**, *17* (9), 5805–5810.

(27) Deng, C.; Huang, Y.; An, M.; Yang, N. Phonon weak couplings model and its applications: A revisit to two-temperature non-equilibrium transport. *Materials Today Physics* **2021**, *16*, 100305.

(28) Pan, D.; Zong, Z.; Yang, N. Phonon weak couplings in nanoscale thermophysics. *Acta Physica Sinica* **2022**, *71* (8), 086302.

(29) Lee, S.; Broido, D.; Esfarjani, K.; Chen, G. Hydrodynamic phonon transport in suspended graphene. *Nat. Commun.* **2015**, *6* (1), 6290.

(30) Callaway, J. Model for Lattice Thermal Conductivity at Low Temperatures. *Phys. Rev.* **1959**, *113* (4), 1046−1051.

(31) Hu, S.; An, M.; Yang, N.; Li, B. Manipulating the temperature dependence of the thermal conductivity of graphene phononic crystal. *Nanotechnology* **2016**, *27* (26), 265702.

(32) Fang, T.; Konar, A.; Xing, H.; Jena, D. Mobility in semiconducting graphene nanoribbons: Phonon, impurity, and edge roughness scattering. *Phys. Rev. B* **2008**, *78* (20), 205403.

(33) Yang, N.; Zhang, G.; Li, B. Violation of Fourier's law and anomalous heat diffusion in silicon nanowires. *Nano Today* **2010**, *5* (2), 85−90.

(34) Liao, Q.; Liu, Z.; Liu, W.; Deng, C.; Yang, N. Extremely High Thermal Conductivity of Aligned Carbon Nanotube-Polyethylene Composites. *Sci. Rep.* **2015**, *5* (1), 16543.

(35) Barbalinardo, G.; Chen, Z.; Dong, H.; Fan, Z.; Donadio, D. Ultrahigh Convergent Thermal Conductivity of Carbon Nanotubes from Comprehensive Atomistic Modeling. *Phys. Rev. Lett.* **2021**, *127* (2), 025902.

(36) Deng, S.; Ma, D.; Zhang, G.; Yang, N. Modulating the thermal conductivity of crystalline nylon by tuning hydrogen bonds through structure poling. *Journal of Materials Chemistry A* **2021**, *9* (43), 24472−24479.

(37) Deng, S.; Yuan, J.; Lin, Y.; Yu, X.; Ma, D.; Huang, Y.; Ji, R.; Zhang, G.; Yang, N. Electric-field-induced modulation of thermal conductivity in poly(vinylidene fluoride). *Nano Energy* **2021**, *82*, 105749.

(38) Yu, X.; Ma, D.; Deng, C.; Wan, X.; An, M.; Meng, H.; Li, X.; Huang, X.; Yang, N. How Does van der Waals Confinement Enhance Phonon Transport? *Chin. Phys. Lett.* **2021**, *38* (1), 014401.

(39) Dames, C. Ultrahigh thermal conductivity confirmed in boron arsenide. *Science* **2018**, *361* (6402), 549−550.

(40) van Roekeghem, A.; Carrete, J.; Oses, C.; Curtarolo, S.; Mingo, N. High-Throughput Computation of Thermal Conductivity of High-Temperature Solid Phases: The Case of Oxide and Fluoride Perovskites. *Physical Review X* **2016**, *6* (4), 041061.

(41) Henry, A.; Chen, G. High Thermal Conductivity of Single Polyethylene Chains Using Molecular Dynamics Simulations. *Phys. Rev. Lett.* **2008**, *101* (23), 235502.

(42) Shen, S.; Henry, A.; Tong, J.; Zheng, R.; Chen, G. Polyethylene nanofibres with very high thermal conductivities. *Nat. Nanotechnol.* **2010**, *5* (4), 251−255.

(43) Katre, A.; Carrete, J.; Dongre, B.; Madsen, G. K. H.; Mingo, N. Exceptionally Strong Phonon Scattering by B Substitution in Cubic SiC. *Phys. Rev. Lett.* **2017**, *119* (7), 075902.

(44) Yamawaki, M.; Ohnishi, M.; Ju, S.; Shiomi, J. Multifunctional structural design of graphene thermoelectrics by Bayesian optimization. *Science Advances* **2018**, *4* (6), No. eaar4192.

(45) An, M.; Li, L.; Hu, S.; Ding, Z.; Yu, X.; Demir, B.; Yang, N.; Ma, W.; Zhang, X. Mass difference and polarization lead to low thermal conductivity of graphene-like carbon nitride (C3N). *Carbon* **2020**, *162*, 202−208.

(46) An, M.; Wang, H.; Yuan, Y.; Chen, D.; Ma, W.; Sharshir, S. W.; Zheng, Z.; Zhao, Y.; Zhang, X. Strong phonon coupling induces low thermal conductivity of one-dimensional carbon boron nanotube. *Surfaces and Interfaces* **2022**, *28*, 101690.

(47) Ma, D.; Arora, A.; Deng, S.; Xie, G.; Shiomi, J.; Yang, N. Quantifying phonon particle and wave transport in silicon nanophononic metamaterial with cross junction. *Materials Today Physics* **2019**, *8*, 56−61.

(48) Yang, L.; Yang, N.; Li, B. Extreme Low Thermal Conductivity in Nanoscale 3D Si Phononic Crystal with Spherical Pores. *Nano Lett.* **2014**, *14* (4), 1734−1738.

(49) Ma, D.; Wan, X.; Yang, N. Unexpected thermal conductivity enhancement in pillared graphene nanoribbon with isotopic resonance. *Phys. Rev. B* **2018**, *98* (24), 245420.

(50) Hussein, M. I.; Tsai, C.-N.; Honarvar, H. Thermal Conductivity Reduction in a Nanophononic Metamaterial versus a Nanophononic Crystal: A Review and Comparative Analysis. *Adv. Funct. Mater.* **2020**, *30* (8), 1906718.

(51) Wan, X.; Ma, D.; Pan, D.; Yang, L.; Yang, N. Optimizing thermal transport in graphene nanoribbon based on phonon resonance hybridization. *Materials Today Physics* **2021**, *20*, 100445.

(52) Zhang, Z.; Guo, Y.; Bescond, M.; Chen, J.; Nomura, M.; Volz, S. Heat Conduction Theory Including Phonon Coherence. *Phys. Rev. Lett.* **2022**, *128* (1), 015901.

(53) An, M.; Chen, D.; Ma, W.; Hu, S.; Zhang, X. Directly visualizing the crossover from incoherent to coherent phonons in two-dimensional periodic MoS2/MoSe2 arrayed heterostructure. *Int. J. Heat Mass Transfer* **2021**, *178*, 121630.

(54) Ma, D.; Ding, H.; Meng, H.; Feng, L.; Wu, Y.; Shiomi, J.; Yang, N. Nano-cross-junction effect on phonon transport in silicon nanowire cages. *Phys. Rev. B* **2016**, *94* (16), 165434.

(55) Davis, B. L.; Hussein, M. I. Nanophononic Metamaterial: Thermal Conductivity Reduction by Local Resonance. *Phys. Rev. Lett.* **2014**, *112* (5), 055505.

(56) Xu, Z.; Baowen, L. Phonon condensation and cooling via nonlinear feedback (2022-01-01); arXiv:2201.00251.

(57) Xu, Y.; Kraemer, D.; Song, B.; Jiang, Z.; Zhou, J.; Loomis, J.; Wang, J.; Li, M.; Ghasemi, H.; Huang, X.; Li, X.; Chen, G. Nanostructured polymer films with metal-like thermal conductivity. *Nat. Commun.* **2019**, *10* (1), 1771.

(58) Dong, L.; Xi, Q.; Zhou, J.; Xu, X.; Li, B. Phonon Renormalization Induced by Electric Field in Ferroelectric Poly(Vinylidene Fluoride−Trifluoroethylene) Nanofibers. *Physical Review Applied* **2020**, *13* (3), 034019.

(59) Yang, L.; Zhang, Q.; Hu, G.; Yang, N. Deformation insensitive thermal conductance of the designed Si metamaterial. *Appl. Phys. Lett.* **2023**, *123* (6), 062201.

(60) Sekiguchi, F.; Hirori, H.; Yumoto, G.; Shimazaki, A.; Nakamura, T.; Wakamiya, A.; Kanemitsu, Y. Enhancing the Hot-Phonon Bottleneck Effect in a Metal Halide Perovskite by Terahertz Phonon Excitation. *Phys. Rev. Lett.* **2021**, *126* (7), 077401.

(61) Bakulin, A. A.; Lovrincic, R.; Yu, X.; Selig, O.; Bakker, H. J.; Rezus, Y. L. A.; Nayak, P. K.; Fonari, A.; Coropceanu, V.; Brédas, J.-L.; Cahen, D. Mode-selective vibrational modulation of charge transport in organic electronic devices. *Nat. Commun.* **2015**, *6* (1), 7880.

(62) Price, M. B.; Butkus, J.; Jellicoe, T. C.; Sadhanala, A.; Briane, A.; Halpert, J. E.; Broch, K.; Hodgkiss, J. M.; Friend, R. H.; Deschler, F. Hot-carrier cooling and photoinduced refractive index changes in organic−inorganic lead halide perovskites. *Nat. Commun.* **2015**, *6* (1), 8420.

(63) Yang, Y.; Ostrowski, D. P.; France, R. M.; Zhu, K.; van de Lagemaat, J.; Luther, J. M.; Beard, M. C. Observation of a hot-phonon bottleneck in lead-iodide perovskites. *Nat. Photonics* **2016**, *10* (1), 53−59.

(64) Yang, J.; Wen, X.; Xia, H.; Sheng, R.; Ma, Q.; Kim, J.; Tapping, P.; Harada, T.; Kee, T. W.; Huang, F.; Cheng, Y.-B.; Green, M.; Ho-Baillie, A.; Huang, S.; Shrestha, S.; Patterson, R.; Conibeer, G. Acoustic-optical phonon up-conversion and hot-phonon bottleneck in lead-halide perovskites. *Nat. Commun.* **2017**, *8* (1), 14120.

(65) Sullivan, S.; Vallabhaneni, A.; Kholmanov, I.; Ruan, X.; Murthy, J.; Shi, L. Optical Generation and Detection of Local Nonequilibrium Phonons in Suspended Graphene. *Nano Lett.* **2017**, *17* (3), 2049−2056.

(66) Wang, R.; Zobeiri, H.; Xie, Y.; Wang, X.; Zhang, X.; Yue, Y. Distinguishing Optical and Acoustic Phonon Temperatures and Their Energy Coupling Factor under Photon Excitation in nm 2D Materials. *Advanced Science* **2020**, *7* (13), 2000097.

(67) Guo, H.; Chu, W.; Prezhdo, O. V.; Zheng, Q.; Zhao, J. Strong Modulation of Band Gap, Carrier Mobility and Lifetime in Two-Dimensional Black Phosphorene through Acoustic Phonon Excitation. *J. Phys. Chem. Lett.* **2021**, *12* (16), 3960−3967.

(68) Gordiz, K.; Muy, S.; Zeier, W. G.; Shao-Horn, Y.; Henry, A. Enhancement of ion diffusion by targeted phonon excitation. *Cell Reports Physical Science* **2021**, *2* (5), 100431.

(69) Itin, A. P.; Katsnelson, M. I. Efficient excitation of nonlinear phonons via chirped pulses: Induced structural phase transitions. *Phys. Rev. B* **2018**, *97* (18), 184304.

(70) Hase, M.; Fons, P.; Mitrofanov, K.; Kolobov, A. V.; Tominaga, J. Femtosecond structural transformation of phase-change materials far from equilibrium monitored by coherent phonons. *Nat. Commun.* **2015**, *6* (1), 8367.

(71) Ward, A.; Broido, D. A.; Stewart, D. A.; Deinzer, G. Ab initio theory of the lattice thermal conductivity in diamond. *Phys. Rev. B* **2009**, *80* (12), 125203.

(72) Rapaport, D. C. *The Art of Molecular Dynamics Simulation*, 2nd ed.; Cambridge University Press: 2004.

(73) Ziman, J. M. *Electrons and phonons: the theory of transport phenomena in solids*; Oxford University Press: 2001.

(74) Kresse, G.; Furthmüller, J. Efficient iterative schemes for ab initio total-energy calculations using a plane-wave basis set. *Phys. Rev. B* **1996**, *54* (16), 11169−11186.

(75) Li, W.; Carrete, J.; Katcho, N. A.; Mingo, N. ShengBTE: A solver of the Boltzmann transport equation for phonons. *Comput. Phys. Commun.* **2014**, *185* (6), 1747−1758.

(76) Han, Z.; Yang, X.; Li, W.; Feng, T.; Ruan, X. FourPhonon: An extension module to ShengBTE for computing four-phonon scattering rates and thermal conductivity. *Comput. Phys. Commun.* **2022**, *270*, 108179.

(77) Togo, A.; Oba, F.; Tanaka, I. First-principles calculations of the ferroelastic transition between rutile-type and ${\text{CaCl}}_{2}$-type ${\text{SiO}}_{2}$ at high pressures. *Phys. Rev. B* **2008**, *78* (13), 134106.

(78) Plimpton, S. Fast Parallel Algorithms for Short-Range Molecular Dynamics. *J. Comput. Phys.* **1995**, *117* (1), 1−19.

(79) Wu, X.; Néel, N.; Brandbyge, M.; Kröger, J. Enhancement of Graphene Phonon Excitation by a Chemically Engineered Molecular Resonance. *Phys. Rev. Lett.* **2023**, *130* (11), 116201.

(80) Balandin, A. A. Thermal properties of graphene and nanostructured carbon materials. *Nat. Mater.* **2011**, *10* (8), 569−581.

(81) Balandin, A. A.; Ghosh, S.; Bao, W.; Calizo, I.; Teweldebrhan, D.; Miao, F.; Lau, C. N. Superior Thermal Conductivity of Single-Layer Graphene. *Nano Lett.* **2008**, *8* (3), 902−907.

(82) Cai, W.; Moore, A. L.; Zhu, Y.; Li, X.; Chen, S.; Shi, L.; Ruoff, R. S. Thermal Transport in Suspended and Supported Monolayer Graphene Grown by Chemical Vapor Deposition. *Nano Lett.* **2010**, *10* (5), 1645−1651.

(83) Lindsay, L.; Li, W.; Carrete, J.; Mingo, N.; Broido, D. A.; Reinecke, T. L. Phonon thermal transport in strained and unstrained graphene from first principles. *Phys. Rev. B* **2014**, *89* (15), 155426.

(84) Xu, X.; Pereira, L. F. C.; Wang, Y.; Wu, J.; Zhang, K.; Zhao, X.; Bae, S.; Tinh Bui, C.; Xie, R.; Thong, J. T. L.; Hong, B. H.; Loh, K. P.; Donadio, D.; Li, B.; Özyilmaz, B. Length-dependent thermal conductivity in suspended single-layer graphene. *Nat. Commun.* **2014**, *5* (1), 3689.

(85) Majumdar, A.; Reddy, P. Role of electron−phonon coupling in thermal conductance of metal−nonmetal interfaces. *Appl. Phys. Lett.* **2004**, *84* (23), 4768−4770.

(86) Liao, B.; Zhou, J.; Chen, G. Generalized Two-Temperature Model for Coupled Phonon-Magnon Diffusion. *Phys. Rev. Lett.* **2014**, *113* (2), 025902.

(87) Zhou, Y.; Hu, M. Quantitatively analyzing phonon spectral contribution of thermal conductivity based on nonequilibrium molecular dynamics simulations. *II. From time Fourier transform, Physical Review B* **2015**, *92* (19), 195205.

(88) Zhou, Y.; Zhang, X.; Hu, M. Quantitatively analyzing phonon spectral contribution of thermal conductivity based on nonequilibrium molecular dynamics simulations, I. From space Fourier transform. *Phys. Rev. B* **2015**, *92* (19), 195204.

(89) Chen, S.; Wu, Q.; Mishra, C.; Kang, J.; Zhang, H.; Cho, K.; Cai, W.; Balandin, A. A.; Ruoff, R. S. Thermal conductivity of isotopically modified graphene. *Nat. Mater.* **2012**, *11* (3), 203−207.

(90) Li, X.; Maute, K.; Dunn, M. L.; Yang, R. Strain effects on the thermal conductivity of nanostructures. *Phys. Rev. B* **2010**, *81* (24), 245318.

(91) Kaviany, M. *Heat transfer physics*; Cambridge University Press: 2014.

(92) Feng, T.; Ruan, X.; Ye, Z.; Cao, B. Spectral phonon mean free path and thermal conductivity accumulation in defected graphene: The effects of defect type and concentration. *Phys. Rev. B* **2015**, *91* (22), 224301.

(93) Hu, S.; Chen, J.; Yang, N.; Li, B. Thermal transport in graphene with defect and doping: Phonon modes analysis. *Carbon* **2017**, *116*, 139−144.

Appendix

Modulating Thermal Conductivity via Targeted Phonon Excitation

Xiao Wan[1#], Dongkai Pan[1#], Zhicheng Zong[1], Yangjun Qin[1], Jing-Tao Lü[2], Sebastian Volz[3,4], Lifa Zhang[5], Nuo Yang[1,6*]

1. School of Energy and Power Engineering, Huazhong University of Science and Technology, Wuhan 430074, China.

2. School of Physics and Wuhan National High Magnetic Field Center, Huazhong University of Science and Technology, Wuhan 430074, China.

3. LIMMS, CNRS-IIS UMI 2820, The University of Tokyo, Tokyo 153-8505, Japan.

4. Institute of Industrial Science, The University of Tokyo, Tokyo 153-8505, Japan.

5. Phonon Engineering Research Center of Jiangsu Province, Ministry of Education Key Laboratory of NSLSCS, Center for Quantum Transport and Thermal Energy Science, Institute of Physics Frontiers and Interdisciplinary Sciences, School of Physics and Technology, Nanjing Normal University, Nanjing 210023, China.

6. Department of Physics, National University of Defense Technology, Changsha 410073, China.

# X.W. and D.P. contributed equally to this work.

*Corresponding email: nuo@hust.edu.cn, nuo@nudt.edu.cn (N.Y)

Appendix A: Ab initio Calculations

The ab initio calculation in this work is based on the Density Functional Theory (DFT) [1, 2], implemented by the Vienna Ab initio Simulation Package (VASP) [3]. The harmonic interatomic force constants (IFCs) are obtained by employing the Density Functional Perturbation Theory (DFPT) [4], while the anharmonic IFCs are treated with the modified ShengBTE code [5]. An 8×8×1 supercell is constructed for the calculations of the harmonic and anharmonic IFCs, and the interactions are taken into account up to the 9th neighbor atoms. The overall thermal conductivity calculation is carried out via an iterative solution of the linearized phonon Boltzmann Transport Equation (BTE) with a Γ-centered 47×47×1 regular grid. It should be noted that the anharmonic interaction is considered up to the 3rd order. As reported in previous works, the 4th order interatomic forces are non-negligible to obtain the exact thermal conductivity value for a monolayer graphene. After including the 4th order interatomic interaction, the thermal conductivity of 9 μm graphene is reduced significantly from 3383 to 810 W m^{-1} K^{-1}, which mainly results from the decreased contribution of the ZA branch [6]. Nevertheless, the focus of this work is not on the quantitative value but rather on the new strategy to tune the thermal conductivity at the quantum level according to phonon scattering rates as well as thermal conductivity contribution. Monolayer graphene has been widely investigated in the past decades due to its superior physical properties and is employed as a demonstrator, to validate the methodology proposed here. Note that the majority of the materials does not exhibit such a strong dependence upon higher order anharmonicity, thus it is not considered here.

The three-phonon scattering rates are obtained from the following Eqs. (1) and (2)

$$\Gamma^{+}_{\lambda\lambda'\lambda''} = \frac{\hbar\pi}{4}\frac{f_0' - f_0''}{\omega_{\lambda}\omega_{\lambda'}\omega_{\lambda''}}\left|V^{+}_{\lambda\lambda'\lambda''}\right|^2\delta(\omega_\lambda + \omega_{\lambda'} - \omega_{\lambda''}) \quad (1)$$

$$\Gamma^{-}_{\lambda\lambda'\lambda''} = \frac{\hbar\pi}{4}\frac{f_0' + f_0'' + 1}{\omega_{\lambda}\omega_{\lambda'}\omega_{\lambda''}}\left|V^{-}_{\lambda\lambda'\lambda''}\right|^2\delta(\omega_\lambda - \omega_{\lambda'} - \omega_{\lambda''}) \quad (2)$$

where $\Gamma^{\pm}_{\lambda\lambda'\lambda''}$ are the three-phonon scattering rates and f_0 stands for the equilibrium phonon distribution function. The manipulation of the scattering rate of a single given mode is achieved by modifying the distribution function, Eq. (3) in the manuscript. Besides, time evolution is not included and the ab-initio calculation of the above formula describes an instantaneous process.

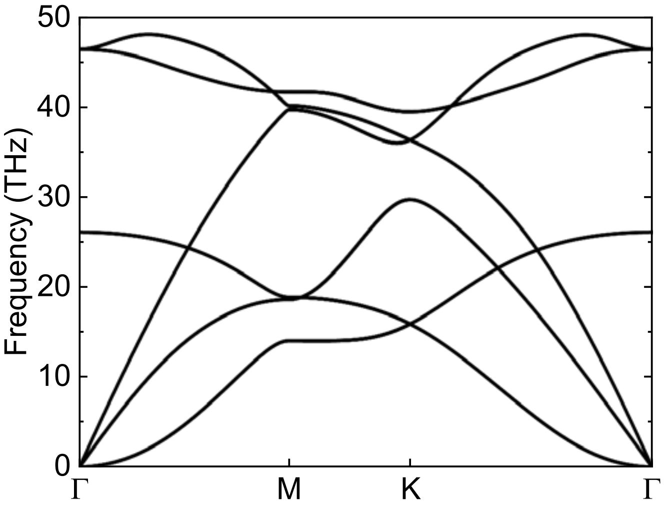

Fig. S1. Phonon dispersion relation in graphene.

As indicated in Fig. S3, the scattering rates increase largely in both cases. But the overall thermal conductivity changes differently in these two cases. This is attributed to the competitive mechanisms of targeted phonon excitation. On one hand, stronger scattering hinders thermal transport. On the other hand, the excitation can enhance thermal transport by increasing the heat capacities of corresponding modes. Specifically, mode specific heat capacity can be expressed as [7]

$$C_n = \left(\frac{\partial E_n}{\partial T}\right)_V \propto \frac{f(f+1)}{T^2} \tag{3}$$

where E_n represents the energy of mode n, T is the absolute temperature and f denotes phonon distribution function. For the targeted modes, the energy after excitation E_n' increases by N times, resulting from the increase in the occupation number of corresponding phonons. Indeed, based on this formula, the energy required to heat these phonons also rises. In essence, the mode specific heat capacity increases accordingly. These excited phonons offer additional pathways for heat transfer, thereby enhancing overall thermal transport, particularly when scattering is minimal. For the modes with dominating contribution to the overall thermal conductivity, the latter factor is more prominent, while for some other modes, the reverse is true.

As for the energy per unit area needed for the excitation, the density of q-points grid is considered to approximate the area of the graphene. A 47×47×1 grid corresponds to a 47×47×1 supercell, which has an area of 116.5 nm^2. The energy needed for each mode is calculated as $\Delta E_n = E_n' - E_n$.

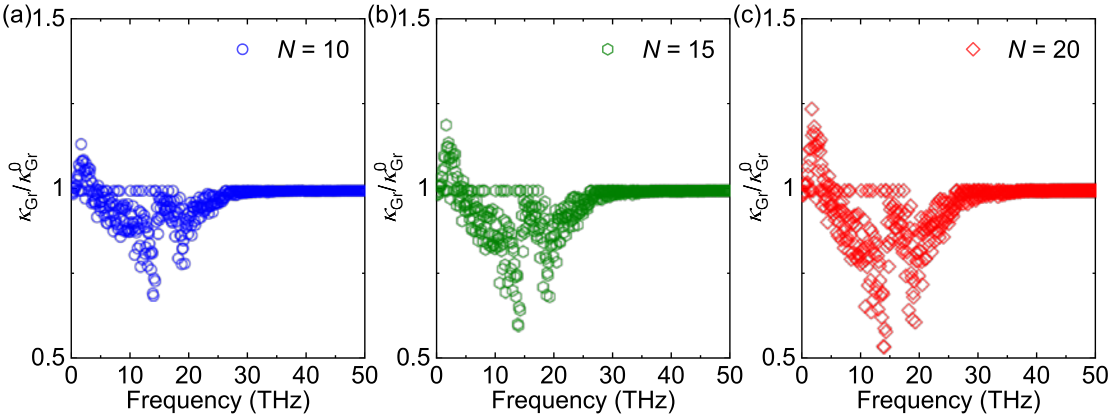

Fig. S2. Thermal conductivity modulation for graphene via targeted phonon excitation. (a−c) The relative overall thermal conductivity of graphene after and before the excitation $\kappa_{\mathrm{Gr}}/\kappa_{\mathrm{Gr}}^0$ as a function of the center frequency for targeted phonons.

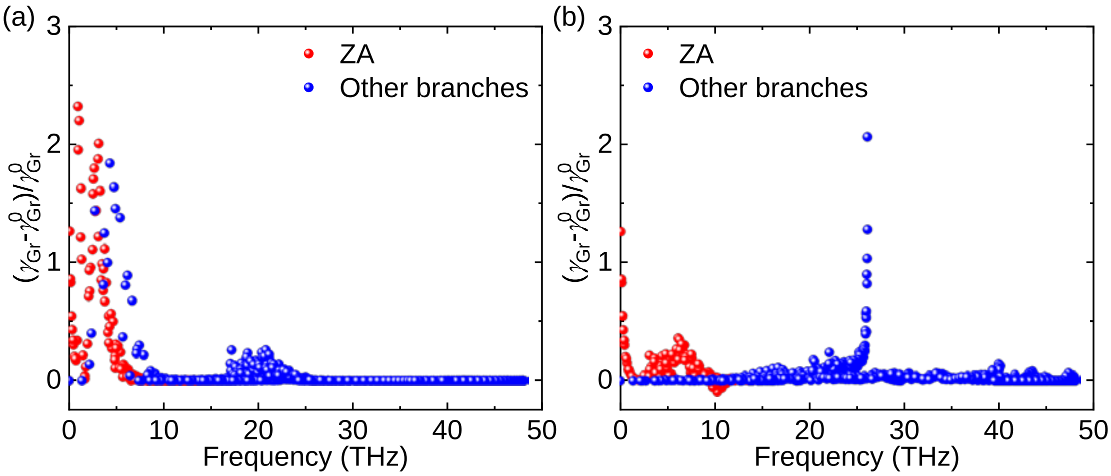

Fig. S3. Scattering rates' changes in graphene by ab initio calculations. (a) The modes in 1.6−1.7 THz are excited with a ten times larger energy, resulting in the highest relative overall thermal conductivity. (b) The modes in 13.9−14.0 THz are excited with a ten times larger energy, leading to the lowest relative overall thermal conductivity.

The thermal conductivity contributions in different cases are depicted in Fig. S4. These values are derived from iterative solutions of the BTE, averaging the effects of exciting targeted phonons [5]. In the peak scenario illustrated in Fig. 2, the observed increase in thermal conductivity primarily arises from the heightened contribution of modes with frequencies below 11.5 THz. Conversely, in the trough case, the reduction in thermal conductivity is associated with modes below 10 THz and those spanning from 19.1 to 24.6 THz. With the targeted phonons involved in more scattering processes, the contribution across a broader frequency range is influenced by the excitation.

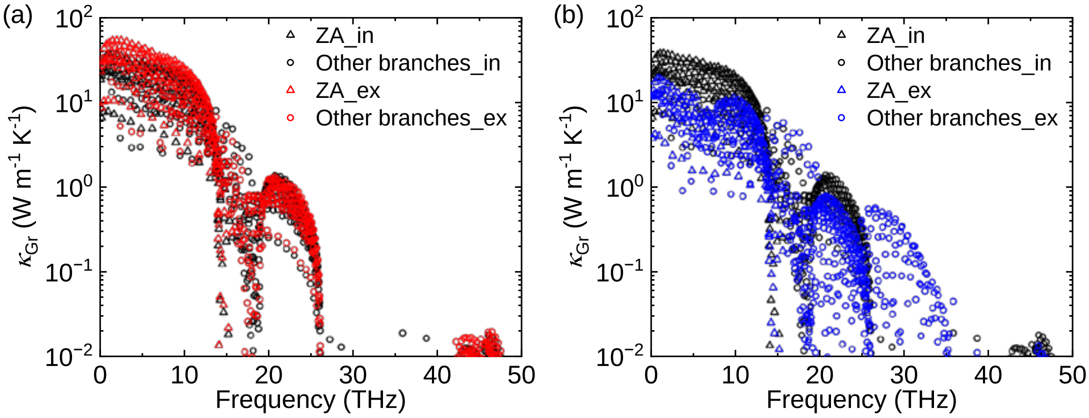

Fig. S4. Thermal conductivity contributions' changes in graphene by ab initio calculations, where 'ex' and 'in' denote the excited and intrinsic cases, respectively. (a) The modes in 1.6−1.7 THz are excited with a twenty-five-times larger energy, resulting in the highest relative overall thermal conductivity. (b) The modes in 13.8−13.9 THz are excited with a twenty-five-times larger energy, leading to the lowest relative overall thermal conductivity.

By DFT calculations, it has been determined that the proposed strategy can yield significant modulating effects on 3D bulk materials, such as silicon at 150 K. The choice of a lower temperature is deliberate, as it leads to weaker phonon couplings compared to room temperature, thereby allowing for a more pronounced modulation effect to be observed.

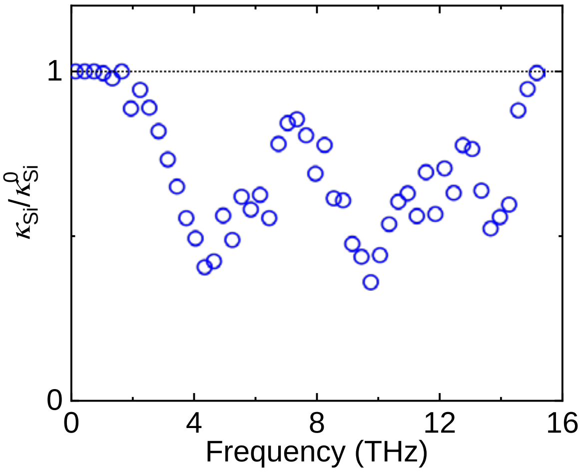

Fig. S5. The relative overall thermal conductivity of silicon after and before the excitation $\kappa_{\mathrm{Si}}/\kappa_{\mathrm{Si}}^{0}$ as a function of the center frequency for targeted phonons. For instance, the first center frequency is 0.15 THz, and a few modes in 0−0.3 THz are excited with a twenty times larger energy.

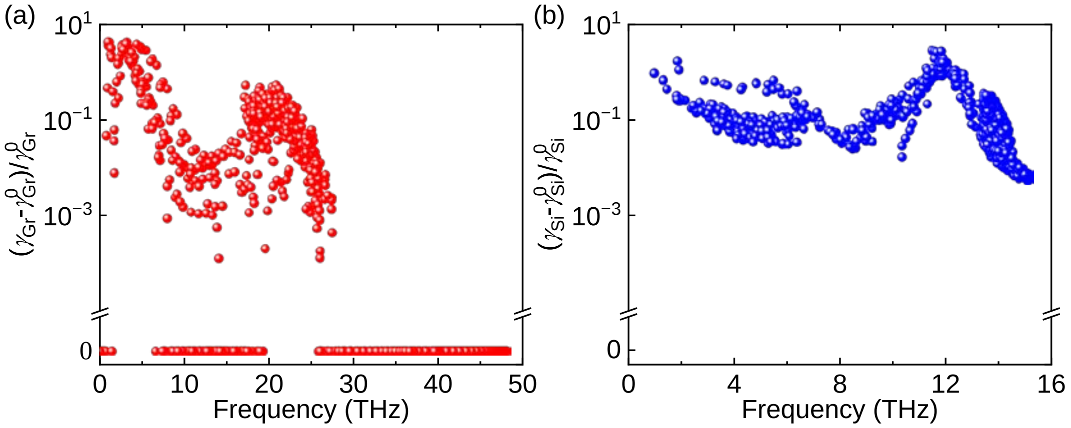

Fig. S6. Scattering rates' changes by ab initio calculations. (a) graphene at 300 K, the modes in 1.6−1.7 THz are excited with a twenty times larger energy. (b) silicon at 150 K, the modes in 1.8−2.1 THz are excited with a twenty times larger energy.

In the case of bulk silicon, the modulation primarily leads to a decrease in thermal conductivity, without a noticeable increase at low frequencies, as illustrated in Fig. S5. This behavior can be attributed to the inherent disparities in phonon coupling mechanisms between 2D and 3D bulk materials. Specifically, in 2D materials, the presence of reflection symmetry weakens the coupling between out-of-plane phonon modes (ZA phonon branch) and in-plane phonon modes. Interestingly, this weakened coupling can actually contribute to enhancing thermal conductivity. To elucidate this weak coupling mechanism, a comparative analysis is presented in Fig. S6. As evident from the figure, a significant number of modes in graphene remain largely unaffected following modulation, while in silicon, the scattering of all modes is enhanced. Notably, these unchanged modes in graphene play a crucial role in contributing to the observed increase in thermal conductivity during modulation. Furthermore, Fig. S5 demonstrates that the excitation of optical modes in silicon leads to noticeable effects, as optical modes are more prominently involved in the three-phonon scattering processes in silicon compared to graphene.

Appendix B: Molecular Dynamics Simulation

Table S1. The parameters in NEMD simulations.

Method	Non-equilibrium MD					
Potential (TERSOFF)						
Function	$E = \frac{1}{2}\sum_{i} \sum_{j(\neq i)} f_C\left(r_{ij}\right)\left[f_R\left(r_{ij}\right) + b_{ij} f_A\left(r_{ij}\right)\right]$ $f_C(r) = \begin{cases} 1: r < R - D \\ \frac{1}{2} - \frac{1}{2} sin\left(\frac{\pi}{2}\frac{r - D}{D}\right): R - D < r < R + D \\ 0: r > R + D \end{cases}$ $f_R(r) = Aexp(-\lambda_1 r)\ \ f_A(r) = -Bexp(-\lambda_2 r)$ $b_{ij} = \left(1 + \beta^n \varsigma_{ij}^n\right)^{-\frac{1}{2n}}$ $\varsigma_{ij} = \sum_{k \neq i,j} f_C\left(r_{ij}\right) g\left(\theta_{ijk}\right) exp\left[\lambda_3^m \left(r_{ij} - r_{ik}\right)^m\right]$ $g(\theta) = \gamma_{ijk}\left(1 + \frac{c^2}{d^2} - \frac{c^2}{[d^2 + (cos\theta - cos\theta_0)^2]}\right)$					
Parameters	m	γ	λ	c	d	$cos\theta$
	3.0	1.0	3.8e4	4.3484	-0.930	0.72751
n	β	λ	B	R	λ	A
1.57e-7	2.2119	430.0	1.95	0.15	3.4879	1393.6
Simulation process						
Ensemble	**Setting**				**Purpose**	
NPT	Runtime (ns)		2		Relax structure	
	Temperature (K)		300			
	Boundary condition		longitudinal, transverse, periodic, periodic			
NVE	Runtime (ns)		100			
	Boundary condition		longitudinal, transverse, fixed, free			
	Thermostat		Heat source	310 K		
			Heat sink	290 K		
NVE	Runtime (ns)		50		Record information	
	Boundary condition		longitudinal, transverse, fixed, free			
	Thermostat		Heat source	310 K		

		Heat sink	290 K	
	Excitation interval	100 fs		
Recorded physical quantity				
Temperature		$\langle E\rangle = \sum_{i=1}^{N}\frac{1}{2}mv_i^2 = \frac{1}{2}Nk_{\mathrm{B}}T_{\mathrm{MD}}$		
Heat flux		$J = \frac{1}{W\cdot d\cdot N_t}\sum_{i=1}^{N_t}\frac{\Delta\varepsilon_i}{2\Delta t}$		
Thermal conductivity		$\kappa = -\frac{J}{\nabla T}$		

In NEMD calculations, the selection of various parameters plays a crucial role in obtaining accurate and reliable results. Parameters such as the time step size, temperature difference, and simulation time require careful consideration. Firstly, the time step size has implications for both the overall CPU running time and the accuracy of the atomic velocity calculation in the simulation. As illustrated in Fig. S7a, a shorter time step leads to increased CPU running time but improves sampling accuracy. Considering previous simulation works [8, 9] and to optimize computational efficiency, we have set the time step to 0.5 fs. Secondly, the temperature difference between the heat source and heat sink affects the temperature gradient in the system. A larger temperature difference results in a more pronounced temperature gradient, but it also has an impact on the non-linear region near the heat bath, as shown in Fig. S7b. Therefore, in this simulation, we selected a temperature difference of 20 K, taking into account previous studies [10, 11]. Thirdly, the intrinsic relaxation time of phonon modes determines the time required for the heat current to reach a steady state. Phonon modes with shorter relaxation times reach steady state more quickly [12]. To ensure the stability of the heat current for low-frequency phonon modes in graphene nanoribbon, a longer total run time (as indicated in Table S1) was chosen, as depicted in Fig. S12.

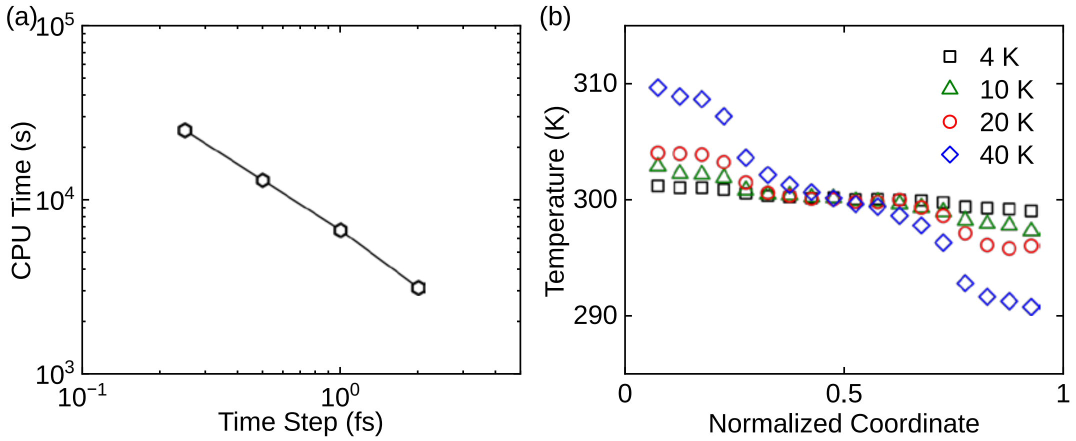

Fig. S7. Assessment of time step and temperature difference in NEMD calculations. (a) Variation of CPU running time with respect to the time step size, keeping the simulation time constant. (b) Temperature profile of graphene nanoribbon at steady state under different temperature differences.

Furthermore, the choice of the rescale factor and excitation intervals also significantly impacts the modulation results in our work. In Fig. S8, it can be observed that as the excitation interval increases, the thermal conductivity after excitation decreases sharply, indicating a weakened modulation effect due to a smaller equivalent input energy density. However, shorter excitation intervals come with higher computational costs. Therefore, we have set the excitation interval to 0.1 ps in this study, striking a balance between computational efficiency and capturing the desired modulation effect. Regarding the rescale factor M, a larger value leads to a greater increase in mode energy, as represented by the multiple of energy increase, N, as shown in Fig. S9. Consequently, a larger rescale factor amplifies the modulation effect. However, it is important to consider the feasibility of experiments and ensure that the equivalent input energy remains within a reasonable range to avoid structural damage. In our study, a rescale factor of $M = 10$ has been chosen for all cases, striking a compromise between achieving a noticeable modulation effect and maintaining structural integrity.

The impact of targeted phonon excitation is closely linked to the excitation interval. As illustrated in Fig. S9, the kinetic energy of the targeted mode rapidly decays after excitation. This behavior aligns with findings from a previous study [13], which suggested that the coupling length between different phonons in graphene is approximately 10 nm. Considering the typical group velocity of graphene, around 10 km/s, this decay occurs on the order of picoseconds, consistent with the trend seen in Fig. S8.

Additionally, it's worth noting that the excitation process occurs at intervals of 100 fs, with an equivalent input energy density ranging from 0.21 to 0.48 mJ m^{-2}. When the excitation interval is extended, there is a sharp decrease in the equivalent input energy density. Consequently, the influence of increased energy gradually diminishes, as depicted in Fig. S8.

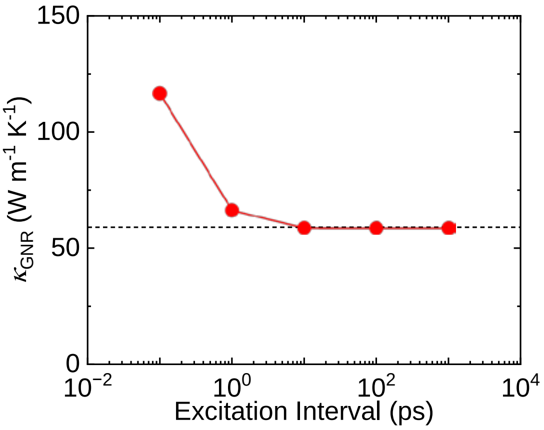

Fig. S8. Modulation of thermal conductivity at different excitation intervals when exciting targeted modes between 9 and 10 THz with a consistent rescale factor. The dashed line represents the intrinsic value.

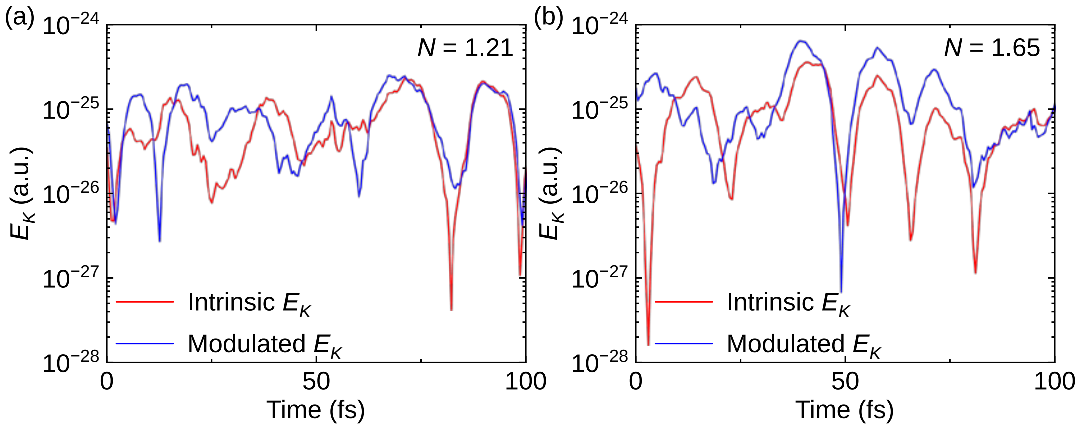

Fig. S9. Time evolution of kinetic energy of the targeted mode before and after excitation, 9.84 THz, $\boldsymbol{k} = (-0.64, 0.96, 0)$, obtained from NEMD simulations. (a) Rescale factor $M = 2$. (b) Rescale factor $M = 5$.

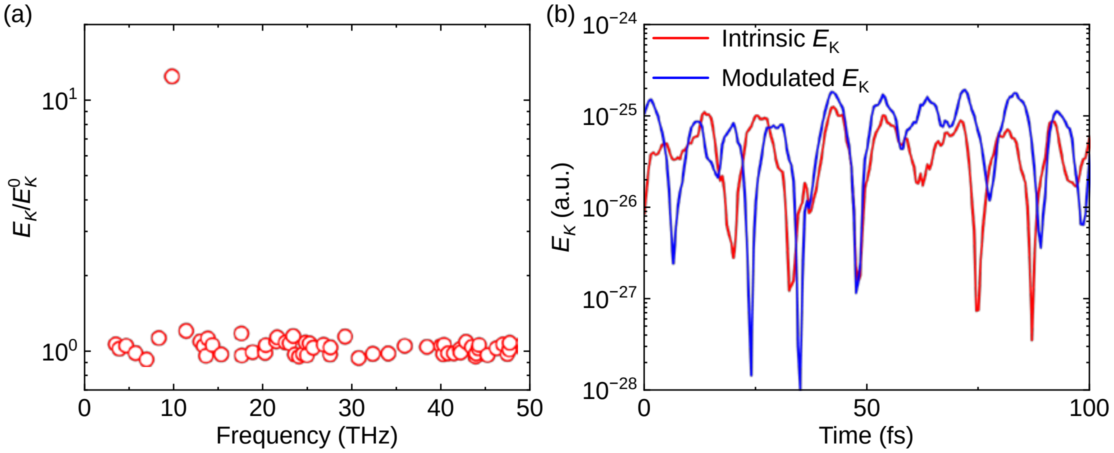

Fig. S10. Kinetic energy of modes in graphene nanoribbon derived from NEMD simulations. (a) Initial relative kinetic energy of modes after and before the excitation ($M = 10$) of the targeted mode, 9.84 THz, $\boldsymbol{k} = (-0.64, 0.96, 0)$. (b) Time evolution of kinetic energy of the targeted mode.

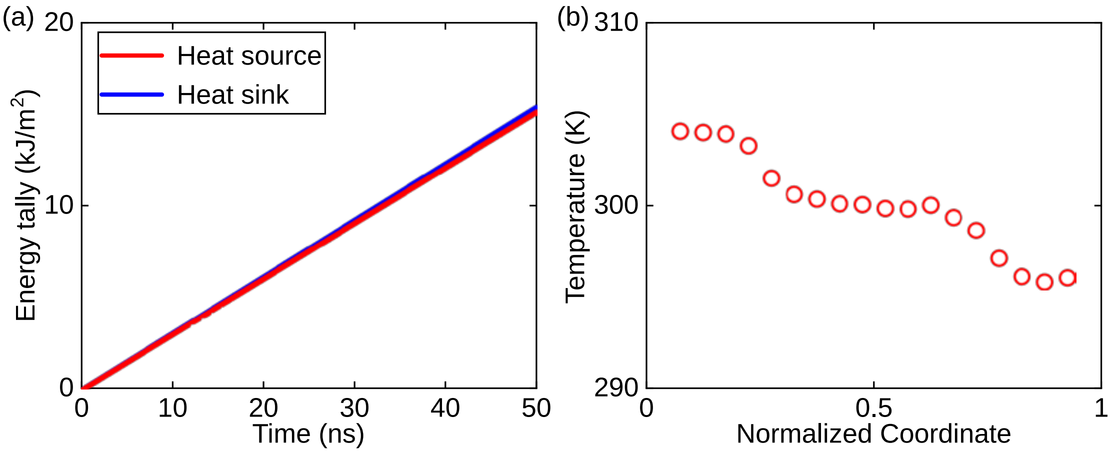

Fig. S11. NEMD results for a graphene nanoribbon where two modes, 9.84 THz, $\boldsymbol{k} = (-0.64, 0.96, 0)$ and 9.84 THz, $\boldsymbol{k} = (0.64, -0.96, 0)$, are excited with a 3.34 times larger kinetic energy (*M* = 10). (a) Energy tallies (i.e., the cumulative energy extracted from the heat sink or added to the heat source) per cross-sectional area. (b) The temperature profile of graphene nanoribbon at steady state. The temperature gradient is taken as the slope of the linear portions of the curves.

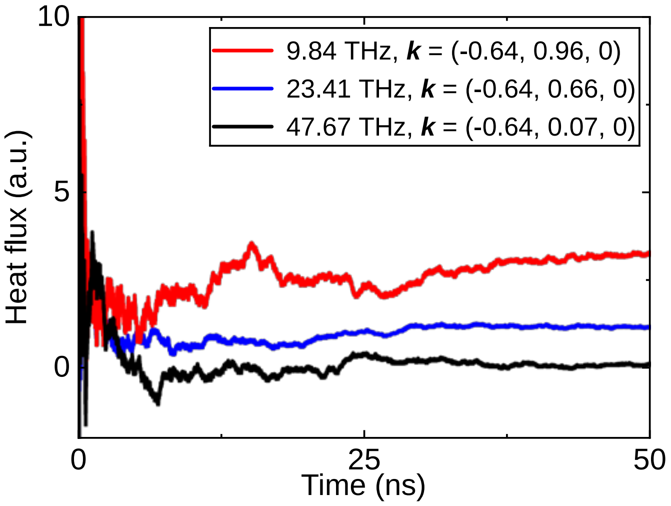

Fig. S12. Heat flux contributions of three typical individual phonon modes of the graphene nanoribbon.

The size effect on the modulation results specifically for the nanoribbon is also investigated. As depicted in Fig. S13, there is a pronounced length dependence in thermal conductivity, primarily attributed to the influence of boundary scattering.

Additionally, the thermal conductivity is also sensitive to the width of the nanoribbon, although the range of widths considered in the calculations was relatively small, resulting in less significant variations. Importantly, the results demonstrate that targeted phonon excitations can effectively modulate the thermal conductivity of larger graphene nanoribbons as well.

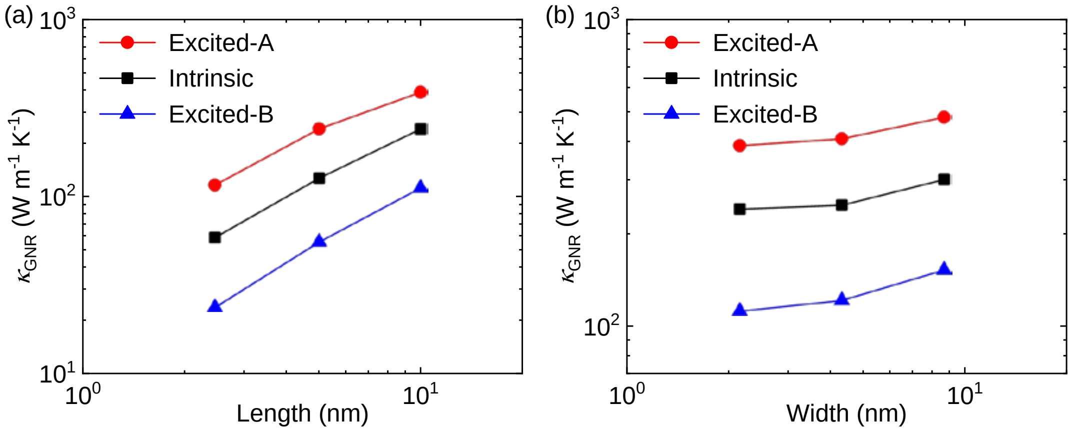

Fig. S13. Size dependence of thermal conductivity in graphene nanoribbons at room temperature. (a) Thermal conductivity versus the length, with the width fixed at 2.16 nm. (b) Thermal conductivity versus the width, with the length maintained at 9.96 nm. The excitation of modes between 9 and 10 THz is denoted as “A” using a common rescale factor, while the excitation of modes between 23 and 24 THz is represented as “B” with the same rescale factor.

Appendix C: Derivation of the Velocity Rescaling Formula

After steady temperature gradient is established, targeted modes are excited based on the following formulation. The velocity equation of any atom can be written as [14]

$$\boldsymbol{v}_j = \sum_n \frac{\dot{Q}_n(t)}{\sqrt{m_j}} \boldsymbol{e}_{j,n} = \sum_n \boldsymbol{v}_{j,n} \tag{4}$$

The individual contribution ($\boldsymbol{v}_{j,n}$) by mode of vibration n to $\boldsymbol{v}_j$ is determined by

$$\boldsymbol{v}_{j,n} = \frac{\dot{Q}_n(t)}{\sqrt{m_j}} \boldsymbol{e}_{j,n} \tag{5}$$

where $\boldsymbol{e}_{j,n}$ is the eigenvector for mode n. And m_j indicate the atomic mass, $\dot{Q}_n$ the normal mode velocity coordinate

$$\dot{Q}_n(t) = \sum_j \sqrt{m_j} \boldsymbol{e}^*_{j,n} \cdot \boldsymbol{v}_j \tag{6}$$

The kinetic energy of mode n is obtained by

$$E_{n,K} = \frac{1}{2} \dot{Q}_n^2 \tag{7}$$

To change the kinetic energy of the normal mode of vibration n to M-fold larger, the mode velocity coordinate is first calculated. Knowing that, for the MD simulation, the atomic velocities are modified by first subtracting the contribution of the component $\boldsymbol{v}_{j,n}$ from $\boldsymbol{v}_j$ and then adding the components that lead to the desired modal kinetic energy,

$$\boldsymbol{v}'_j = \boldsymbol{v}_j - \frac{1}{\sqrt{m_j}} \dot{Q}_n(t) \boldsymbol{e}_{j,n} + \sqrt{\frac{M}{m_j}} \dot{Q}_n(t) \boldsymbol{e}_{j,n} \tag{8}$$

which is simplified as

$$\boldsymbol{v}'_j = \boldsymbol{v}_j + \frac{1}{\sqrt{m_j}} \left(\sqrt{M} - 1\right) \dot{Q}_n(t) \boldsymbol{e}_{j,n} \tag{9}$$

Appendix D: Derivation of the Two-temperature Model

In the two-temperature model [13, 15-17], it's assumed that the excited phonon group is in an equilibrium state, while the other intrinsic phonons are also in their respective equilibriums. Additionally, the mutual influence resulting from the weak coupling between these two groups of phonons is also considered.

The Boltzmann transport equation (BTE) for excited phonons and intrinsic phonons that determines the phonon distribution function is written separately as

$$\frac{\partial f_{\mathrm{ex}}}{\partial t} + \mathbf{F} \cdot \nabla_{\mathrm{p}} f_{\mathrm{ex}} + \mathbf{v} \cdot \nabla_{\mathbf{r}} f_{\mathrm{ex}} = \left(\frac{\partial f_{\mathrm{ex}}}{\partial t}\right)_{\mathrm{c}} \tag{10}$$

$$\frac{\partial f_{\mathrm{in}}}{\partial t} + \mathbf{F} \cdot \nabla_{\mathrm{p}} f_{\mathrm{in}} + \mathbf{v} \cdot \nabla_{\mathbf{r}} f_{\mathrm{in}} = \left(\frac{\partial f_{\mathrm{in}}}{\partial t}\right)_{\mathrm{c}} \tag{11}$$

where the subscripts 'ex' and 'in' denote excited phonons and intrinsic phonons, respectively.

When the system reaches steady state without applying external force, the Eq. (10) and Eq. (11) can be simplified as

$$\mathbf{v} \cdot \nabla_{\mathbf{r}} f_{\mathrm{ex}} = \left(\frac{\partial f_{\mathrm{ex}}}{\partial t}\right)_{\mathrm{c}} \tag{12}$$

$$\mathbf{v} \cdot \nabla_{\mathbf{r}} f_{\mathrm{in}} = \left(\frac{\partial f_{\mathrm{in}}}{\partial t}\right)_{\mathrm{c}} \tag{13}$$

where the right-hand sides are the collision term, which includes three kinds of phonon scattering processes: ex-ex scatterings, in-in scatterings, and scatterings between excited phonons and intrinsic phonons. Based on the assumption above, the collision term can be written as

$$\mathbf{v} \cdot \nabla_{\mathbf{r}} f_{\mathrm{ex}} = \left(\frac{\partial f_{\mathrm{ex}}}{\partial t}\right)_{\mathrm{ex,in}} + \left(\frac{\partial f_{\mathrm{ex}}}{\partial t}\right)_{\mathrm{ex,ex}} \tag{14}$$

$$\mathbf{v} \cdot \nabla_{\mathbf{r}} f_{\mathrm{in}} = \left(\frac{\partial f_{\mathrm{in}}}{\partial t}\right)_{\mathrm{ex,in}} + \left(\frac{\partial f_{\mathrm{in}}}{\partial t}\right)_{\mathrm{in,in}} \tag{15}$$

where the subscripts 'ex,ex', 'in,in', 'ex,in' denote ex-ex scatterings, in-in scatterings, and ex-in scatterings, respectively. When the relaxation time approximation (RTA) is adopted for ex-ex scatterings, in-in scatterings, Eq. (14) and Eq. (15) can be written as

$$\mathbf{v}\cdot\nabla_{\mathrm{r}}f_{\mathrm{ex}}=\left(\frac{\partial f_{\mathrm{ex}}}{\partial t}\right)_{\mathrm{ex,in}}+\left(\frac{f_{\mathrm{ex}}-f_{\mathrm{ex,0}}}{\tau_{\mathrm{ex,ex}}}\right)_{\mathrm{ex,ex}} \tag{16}$$

$$\mathbf{v}\cdot\nabla_{\mathrm{r}}f_{\mathrm{in}}=\left(\frac{\partial f_{\mathrm{in}}}{\partial t}\right)_{\mathrm{ex,in}}+\left(\frac{f_{\mathrm{in}}-f_{\mathrm{in,0}}}{\tau_{\mathrm{in,in}}}\right)_{\mathrm{in,in}} \tag{17}$$

where $f_{\mathrm{ex,0}}$ and $f_{\mathrm{in,0}}$ are the excited phonon and intrinsic phonon distribution function at equilibrium, respectively. $\tau_{\mathrm{ex,ex}}$ and $\tau_{\mathrm{in,in}}$ are the relaxation time for excited phonons and intrinsic phonons, respectively.

After multiplying Eq. (16) and Eq. (17) by $\hbar\omega$, and integrating over all wavevector $\mathbf{q}$, the last terms on the right-hand sides of Eq. (16) and Eq. (17) drop out because they are odd function with respect to all wavevector $\mathbf{q}$, as

$$\nabla_{\mathbf{r}}\cdot\sum_{\mathbf{q}}\hbar\omega_{\mathbf{q}}\mathbf{v}f_{\mathrm{ex}}=\sum_{\mathbf{q}}\hbar\omega_{\mathbf{q}}\left(\frac{\partial f_{\mathrm{ex}}}{\partial t}\right)_{\mathrm{ex,in}} \tag{18}$$

$$\nabla_{\mathbf{r}}\cdot\sum_{\mathbf{q}}\hbar\omega_{\mathbf{q}}\mathbf{v}f_{\mathrm{in}}=\sum_{\mathbf{q}}\hbar\omega_{\mathbf{q}}\left(\frac{\partial f_{\mathrm{in}}}{\partial t}\right)_{\mathrm{ex,in}} \tag{19}$$

Then, it can also be written as

$$\nabla\cdot\mathbf{J}_{\mathrm{ex}}=-\frac{\partial E_{\mathrm{ex}}}{\partial t} \tag{20}$$

$$\nabla\cdot\mathbf{J}_{\mathrm{in}}=-\frac{\partial E_{\mathrm{in}}}{\partial t} \tag{21}$$

The scatterings between ex-in are responsible for the energy exchange between ex and in. $1/\tau_{\mathrm{ex,in}}$ is used to describe the scattering rate for the coupling between ex and in. Then, the rate of energy transfer between ex and in is described by

$$\frac{\Delta E_{\mathrm{ex}}}{\Delta t}=\frac{c_{\mathrm{ex}}(T_{\mathrm{inter}}-T_{\mathrm{ex}})}{\tau_{\mathrm{ex,in}}}=\frac{c_{\mathrm{ex}}c_{\mathrm{in}}(T_{\mathrm{in}}-T_{\mathrm{ex}})}{\tau_{\mathrm{ex,in}}(c_{\mathrm{ex}}+c_{\mathrm{in}})}=G_{\mathrm{ex,in}}(T_{\mathrm{in}}-T_{\mathrm{ex}}) \tag{22}$$

$$\frac{\Delta E_{\mathrm{in}}}{\Delta t}=\frac{c_{\mathrm{in}}(T_{\mathrm{inter}}-T_{\mathrm{in}})}{\tau_{\mathrm{ex,in}}}=\frac{c_{\mathrm{ex}}c_{\mathrm{in}}(T_{\mathrm{ex}}-T_{\mathrm{in}})}{\tau_{\mathrm{ex,in}}(c_{\mathrm{ex}}+c_{\mathrm{in}})}=G_{\mathrm{ex,in}}(T_{\mathrm{ex}}-T_{\mathrm{in}}) \tag{23}$$

$$G_{\mathrm{ex,in}}=\frac{c_{\mathrm{ex}}c_{\mathrm{in}}}{\tau_{\mathrm{ex,in}}(c_{\mathrm{ex}}+c_{\mathrm{in}})} \tag{24}$$

where the intermediate temperature that both channels approach is $T_{\mathrm{inter}}=\frac{c_{\mathrm{ex}}T_{\mathrm{ex}}+c_{\mathrm{in}}T_{\mathrm{in}}}{c_{\mathrm{ex}}+c_{\mathrm{in}}}$. And $G_{\mathrm{ex,in}}$ is defined as the coupling factor.

Then, the Eq. (20) and Eq. (21) can be written as

$$\nabla \mathbf{J}_{\mathrm{ex}} = G_{\mathrm{ex,in}}(T_{\mathrm{in}} - T_{\mathrm{ex}}) \tag{25}$$

$$\nabla \mathbf{J}_{\mathrm{in}} = G_{\mathrm{ex,in}}(T_{\mathrm{ex}} - T_{\mathrm{in}}) \tag{26}$$

Applying the Fourier Law $\mathbf{J} = \kappa \nabla T$ to rewrite Eq. (25) and Eq. (26) as

$$-\kappa_{\mathrm{ex}} \nabla^2 T_{\mathrm{ex}} = G_{\mathrm{ex,in}}(T_{\mathrm{in}} - T_{\mathrm{ex}}) \tag{27}$$

$$-\kappa_{\mathrm{in}} \nabla^2 T_{\mathrm{in}} = G_{\mathrm{ex,in}}(T_{\mathrm{ex}} - T_{\mathrm{in}}) \tag{28}$$

Considering the one-dimensional temperature gradient in the system, the governing equations for coupled phonon transport states

$$-\kappa_{\mathrm{ex}} \frac{d^2 T_{\mathrm{ex}}}{dx^2} = G_{\mathrm{ex,in}}(T_{\mathrm{in}} - T_{\mathrm{ex}}) \tag{29}$$

$$-\kappa_{\mathrm{in}} \frac{d^2 T_{\mathrm{in}}}{dx^2} = G_{\mathrm{ex,in}}(T_{\mathrm{ex}} - T_{\mathrm{in}}) \tag{30}$$

Subtracting Eq. (29) from Eq. (30), it can obtain that

$$\frac{d^2 \theta}{dx^2} - \gamma^2 \theta = 0 \tag{31}$$

where $\theta = T_{\mathrm{ex}} - T_{\mathrm{in}}$ and $\gamma = \sqrt{G_{\mathrm{ex,in}} \left(\frac{1}{\kappa_{\mathrm{ex}}} + \frac{1}{\kappa_{\mathrm{in}}} \right)}$. On the basis of the boundary condition $\theta|_{x=0} = \theta_0$ and $\theta|_{x \to \infty} = 0$, the temperature difference profile is written as $\theta = \theta_0 exp(-\gamma x)$. Using this in Eq. (29), it gets

$$\kappa_{\mathrm{ex}} \frac{d^2 T_{\mathrm{ex}}}{dx^2} = G_{\mathrm{ex,in}} \theta_0 e^{-\gamma x} \tag{32}$$

which can be solved to get the excited phonon temperature profile

$$T_{\mathrm{ex}} = \frac{G_{\mathrm{ex,in}}}{\kappa_{\mathrm{ex}} \gamma^2} \theta_0 e^{-\gamma x} + Cx + D \tag{33}$$

Using the boundary condition for excited phonons, $dT_{\mathrm{ex}}/dx\,|_{x=0} = 0$, the two phonon group temperature profiles are

$$T_{\mathrm{ex}} = \frac{G_{\mathrm{ex,in}}}{\kappa_{\mathrm{ex}} \gamma^2} \theta_0 e^{-\gamma x} + \frac{G_{\mathrm{ex,in}}}{\kappa_{\mathrm{ex}} \gamma} \theta_0 x + D \tag{34}$$

$$T_{\mathrm{in}} = \left(\frac{G_{\mathrm{ex,in}}}{\kappa_{\mathrm{ex}} \gamma^2} - 1 \right) \theta_0 e^{-\gamma x} + \frac{G_{\mathrm{ex,in}}}{\kappa_{\mathrm{ex}} \gamma} \theta_0 x + D \tag{35}$$

Hence, the heat flux can be written as

$$\mathbf{J} = -\kappa_{\mathrm{ex}} \frac{dT_{\mathrm{ex}}}{dx}|_{x=0} - \kappa_{\mathrm{in}} \frac{dT_{\mathrm{in}}}{dx}|_{x=0} = -\kappa_{\mathrm{in}} \frac{dT_{\mathrm{in}}}{dx}|_{x=0} \tag{36}$$

The equivalent thermal conductivity, κ, can be defined as

$$\kappa = \frac{\mathbf{J}}{-\frac{dT_{inter}}{dx}} = \frac{\kappa_{\mathrm{ex}} + \kappa_{\mathrm{in}}}{1 - \left[\frac{c_{\mathrm{ex}}}{c_{\mathrm{ex}} + c_{\mathrm{in}}} - \frac{c_{\mathrm{in}}\kappa_{\mathrm{ex}}}{(c_{\mathrm{ex}} + c_{\mathrm{in}})\kappa_{\mathrm{in}}}\right] e^{-\gamma x}} \tag{37}$$

Now considering the length of the system, $e^{-\gamma x}$ approaches a constant. c_{ex} and c_{in} can be calculated as

$$c_{\mathrm{ex}} = \frac{1}{k_{\mathrm{B}} T_{\mathrm{ex},0}^2 \Omega N} \sum_{\mathbf{q}} f_{\mathrm{ex},0}\left(f_{\mathrm{ex},0} + 1\right) \hbar\omega_{\mathbf{q},\mathrm{ex}} \tag{38}$$

$$c_{\mathrm{in}} = \frac{1}{k_{\mathrm{B}} T_{\mathrm{in},0}^2 \Omega N} \sum_{\mathbf{q}} f_{\mathrm{in},0}\left(f_{\mathrm{in},0} + 1\right) \hbar\omega_{\mathbf{q},\mathrm{in}} \tag{39}$$

where Ω represents the volume of the unit cell, and N denotes the number of $\mathbf{q}$ points. $f_{\mathrm{ex},0}$ is calculated using Eq. (3) as detailed in the manuscript. The thermal conductivity in the α direction can be written as

$$\kappa_{ex}^{\alpha} = \frac{1}{k_{\mathrm{B}} T_{\mathrm{ex},0}^2 \Omega N} \sum_{\mathbf{q}} f_{\mathrm{ex},0}\left(f_{\mathrm{ex},0} + 1\right) \left(\hbar\omega_{\mathbf{q},\mathrm{ex}}\right)^2 v_{\mathbf{q},\mathrm{ex}}^{\alpha} F_{\mathbf{q},\mathrm{ex}}^{\alpha} \tag{40}$$

$$\kappa_{in}^{\alpha} = \frac{1}{k_{\mathrm{B}} T_{\mathrm{in},0}^2 \Omega N} \sum_{\mathbf{q}} f_{\mathrm{in},0}\left(f_{\mathrm{in},0} + 1\right) \left(\hbar\omega_{\mathbf{q},\mathrm{in}}\right)^2 v_{\mathbf{q},\mathrm{in}}^{\alpha} F_{\mathbf{q},\mathrm{in}}^{\alpha} \tag{41}$$

$$F_{\mathbf{q}}^{\alpha} = \tau_{\mathbf{q}} v_{\mathbf{q}}^{\alpha} \tag{42}$$

By using the group velocity $v_{\mathbf{q}}^{\alpha}$ and relaxation time $\tau_{\mathbf{q}}$ from the previous results, κ_{ex} and κ_{in} can be obtained. Subsequently, these values are substituted into the Eq. (37) to estimate κ, which is approximately 4,265 W m^{-1} K^{-1}. It's worth noting that there are acceptable discrepancies of about 4.2% when compared to the original results (4,093 W m^{-1} K^{-1}). These variations can be attributed to an insufficient consideration of nonequilibrium phenomena between different phonon groups.

References

[1] P. Hohenberg, W. Kohn, Inhomogeneous Electron Gas, Physical Review, 136(3B) (1964) B864-B871.

[2] W. Kohn, L.J. Sham, Self-Consistent Equations Including Exchange and Correlation Effects, Physical Review, 140(4A) (1965) A1133-A1138.

[3] G. Kresse, J. Furthmüller, Efficient iterative schemes for ab initio total-energy calculations using a plane-wave basis set, Physical Review B, 54(16) (1996) 11169-11186.

[4] S. Baroni, S. de Gironcoli, A. Dal Corso, P. Giannozzi, Phonons and related crystal properties from density-functional perturbation theory, Reviews of Modern Physics, 73(2) (2001) 515-562.

[5] W. Li, J. Carrete, N. A. Katcho, N. Mingo, ShengBTE: A solver of the Boltzmann transport equation for phonons, Computer Physics Communications, 185(6) (2014) 1747-1758.

[6] T. Feng, X. Ruan, Four-phonon scattering reduces intrinsic thermal conductivity of graphene and the contributions from flexural phonons, Physical Review B, 97(4) (2018) 045202.

[7] M. Kaviany, Heat transfer physics, Cambridge University Press, 2014.

[8] Z. Guo, D. Zhang, X.-G. Gong, Thermal conductivity of graphene nanoribbons, Applied Physics Letters, 95(16) (2009) 163103.

[9] C. Yu, G. Zhang, Impacts of length and geometry deformation on thermal conductivity of graphene nanoribbons, Journal of Applied Physics, 113(4) (2013) 044306.

[10] D. Ma, X. Wan, N. Yang, Unexpected thermal conductivity enhancement in pillared graphene nanoribbon with isotopic resonance, Physical Review B, 98(24) (2018) 245420.

[11] X. Wan, D. Ma, D. Pan, L. Yang, N. Yang, Optimizing thermal transport in graphene nanoribbon based on phonon resonance hybridization, Materials Today Physics, 20 (2021) 100445.

[12] Y. Zhou, X. Zhang, M. Hu, Quantitatively analyzing phonon spectral contribution of thermal conductivity based on nonequilibrium molecular dynamics simulations. I. From space Fourier transform, Physical Review B, 92(19) (2015) 195204.

[13] M. An, Q. Song, X. Yu, H. Meng, D. Ma, R. Li, Z. Jin, B. Huang, N. Yang, Generalized Two-Temperature Model for Coupled Phonons in Nanosized Graphene, Nano Letters, 17(9) (2017) 5805-5810.

[14] M.T. Dove, Introduction to Lattice Dynamics, Cambridge University Press, Cambridge, 1993.

[15] A. Majumdar, P. Reddy, Role of electron–phonon coupling in thermal conductance of metal–nonmetal interfaces, Applied Physics Letters, 84(23) (2004) 4768-4770.

[16] B. Liao, J. Zhou, G. Chen, Generalized Two-Temperature Model for Coupled Phonon-Magnon Diffusion, Physical Review Letters, 113(2) (2014) 025902.

[17] J. Chen, X. Xu, J. Zhou, B. Li, Interfacial thermal resistance: Past, present, and future, Reviews of Modern Physics, 94(2) (2022) 025002.